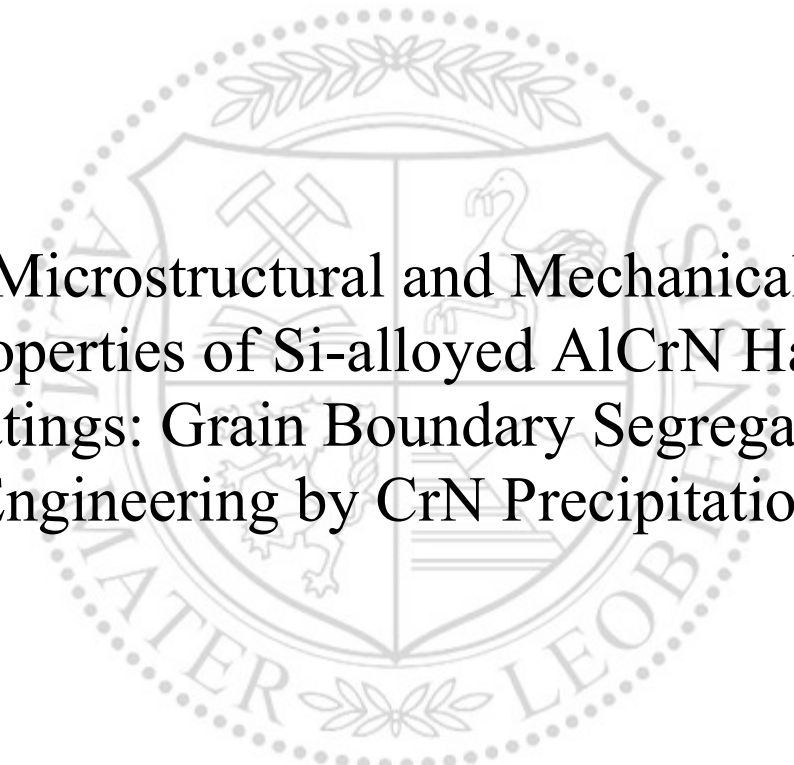




Chair of Materials Physics

Master's Thesis



Microstructural and Mechanical  
Properties of Si-alloyed AlCrN Hard  
Coatings: Grain Boundary Segregation  
Engineering by CrN Precipitation

Tobias Ziegelwanger, BSc

May 2021

# Affidavit

---

I declare, in lieu of oath, that I wrote this thesis and performed the associated research myself, using only literature cited in this volume.

Leoben, May 2020



Tobias Ziegelwanger

# Eidesstaatliche Erklärung

---

Ich erkläre an Eides statt, dass ich diese Arbeit selbständig verfasst, andere als die angegebenen Quellen und Hilfsmittel nicht benutzt, und mich auch sonst keiner unerlaubten Hilfsmittel bedient habe.

Leoben, Mai 2020



Tobias Ziegelwanger

# Danksagung

Allen voran danke ich Univ.-Prof. Jozef Keckes, dass er mich vor 6 Jahren in seine Gruppe aufgenommen hat und meine Ausbildung an der Montanuniversität durch eine beträchtliche Menge an Praxis-Erfahrung, ergänzt hat. Ich danke ihm zudem im Besonderen für die Betreuung dieser Arbeit und die Bereitstellung der notwendigen Mittel zu deren Durchführung.

Dr. Michael Meindlhumer danke ich für die Inspiration zu dieser Arbeit, seiner durchgängigen Betreuung währenddessen. Insbesondere für seinen freundschaftlichen und fachlichen Rat, ohne welchen sie nicht zustande gekommen wäre.

Nikolaus Jäger, MSc. möchte ich für das Bereitstellen der in dieser Arbeit verwendeten Proben danken.

Ich danke des Weiteren meinen Kollegen Sabine Bodner, Juraj Todt und Jakub Zalesak für die vielen Bereichernden Gespräche und Diskussionen im Arbeitsalltag.

Zum Schluss möchte ich meiner Familie Robert, Regina und Sarah Ziegelwanger dafür danken, dass sie mir dieses Studium ermöglicht haben und mir mit ihrem Glauben an mich die Kraft gegeben haben dieses auch zu absolvieren.

# Abstract

---

In the race for hard and simultaneously tough hard coatings, for applications in the metal cutting industry, this thesis takes aim to propose grain boundary segregation engineering as a viable tool to improve mechanical properties of well-established Transition Metal Nitrides, such as AlCrN.

Therefore, in a first step a gradient coating with increasing Si content was deposited by cathodic arc evaporation. This coating was annealed at different temperatures of up to 1100 °C and characterized by cross sectional X-ray nanodiffraction (CSnanoXRD) at the synchrotron source PETRA III at the German Synchrotron (DESY). Measured intensity plots of wide-angle X-ray scattering (WAXS) revealed the formation of a wurtzite (w-) AlN phase with cubic (c-) CrN precipitates and the formation of a nanocomposite structure after alloying with Si. Additionally, small-angle X-ray scattering (SAXS) data indicated the formation of 12 nm thick nanolayers in the Si-free zone of the coating, which abruptly changes to a periodicity of 25 nm after the introduction of Si.

This data collected from the gradient coating was further used for the design of two reference coatings with a composition of  $\text{Al}_{0,8}\text{Cr}_{0,2}\text{N}$  and  $(\text{Al}_{0,7}\text{Cr}_{0,3})_{0,9}\text{Si}_{0,1}\text{N}$  and two additional multilayered coatings of alternating composition of the two reference ones. These four coatings were tested for their mechanical properties by *in situ* cantilever bending experiments and displayed fracture stresses of up to 4.8 GPa and fracture toughness values of up to  $2.8 \text{ MPam}^{1/2}$ .

Through this effort we provide information on the importance of precise annealing parameters when dealing with grain boundary segregation engineering as well as limits that are inherent to this method.

# Zusammenfassung

---

Im modernen Wettlauf um gleichzeitig harte und zähe Hartstoffschichten für den Einsatz in der spanabhebenden Industrie zielt diese Arbeit darauf ab, die Segregation von Korngrenzenphasen als praktikables Werkzeug für etablierte Übergangsmetallnitride, wie AlCrN, zu etablieren.

Dazu wurde in einem ersten Schritt eine Gradientenschicht mit steigendem Si-Gehalt durch kathodische Lichtbogenverdampfung abgeschieden. Diese Schicht wurde bei verschiedenen Temperaturen bis 1100 °C gegläht und mittels Röntgen-Nanodiffraktion (CSnanoXRD) an der Synchrotronquelle PETRA III des Deutschen Synchrotron (DESY) charakterisiert. Gemessene Intensitätsplots der Weitwinkel-Röntgenstreuung (WAXS) zeigten die Bildung einer wurtzitischen (w-) AlN-Phase mit Ausscheidungen von kubischem (c-) CrN und die Ausbildung einer Nanokompositstruktur mit zunehmendem Si-Gehalt. Zusätzlich zeigten Intensitätsplots der Kleinwinkel-Röntgenstreuung (SAXS) die Bildung von 12 nm großen Nanoschichten in der Si-freien Zone nach der Beschichtung, die nach der Einführung von Si abrupt in eine Periodizität von 25 nm übergeht.

Diese Informationen wurden weiter für die Abscheidung von zwei Referenzschichten mit einer Zusammensetzung von  $\text{Al}_{0,8}\text{Cr}_{0,2}\text{N}$  und  $(\text{Al}_{0,7}\text{Cr}_{0,3})_{0,9}\text{Si}_{0,1}\text{N}$ , sowie zur Abscheidung von zwei weiteren Schichten mit einer Mehrlagen-Struktur, bestehend aus abwechselnden Zusammensetzungen der beiden Referenzschichten, verwendet. Diese Beschichtungen wurden in Form von *in situ* Biegebalken Beanspruchung auf ihre mechanischen Eigenschaften getestet und zeigten Bruchspannungen von bis zu 4.8 GPa und Bruchzähigkeitswerte von bis zu 2.8 MPam<sup>1/2</sup>.

Im Rahmen dieser Arbeit geben wir damit Aufschluss über die Bedeutung präziser Glühparameter für die Segregation von Korngrenzenphasen sowie über Grenzen, die dieser Methode inhärent sind.

# Table of Content

<b><i>Danksagung</i></b> .....	<b>1</b>
<b><i>Abstract</i></b> .....	<b>2</b>
<b><i>Zusammenfassung</i></b> .....	<b>3</b>
<b><i>Introduction</i></b> .....	<b>5</b>
Hard Coatings of transition metal nitrides.....	5
Grain Boundary Segregation Engineering.....	7
Thesis Objective .....	9
<b><i>Methods</i></b> .....	<b>10</b>
Physical Vapour Deposition (PVD).....	10
Heat Treatment .....	11
Focused Ion Beam machining (FIB).....	11
Scanning Electron Microscopy (SEM) .....	12
Cross-sectional X-ray nanodiffraction (CSnanoXRD).....	12
Cross Sectional Nanoindentation .....	18
<i>In situ</i> Cantilever Bending .....	20
<b><i>Results</i></b> .....	<b>25</b>
Electron Dispersive X-ray Spectroscopy.....	25
Cross-Sectional Microstructural SEM analysis.....	27
Cross-Sectional X-ray Nanodiffraction – WAXS.....	31
Cross-Sectional X-ray Nanodiffraction – SAXS .....	36
Cross Sectional Nanoindentation .....	40
Microstructural analysis and <i>ex situ</i> fractography.....	42
Mechanical properties obtained by <i>in situ</i> cantilever bending.....	50
<b><i>Discussion</i></b> .....	<b>54</b>
<b><i>Conclusion and Outlook</i></b> .....	<b>58</b>
<b><i>References</i></b> .....	<b>59</b>
<b><i>Index of Figures</i></b> .....	<b>63</b>
<b><i>Index of Tables</i></b> .....	<b>65</b>

## Hard Coatings of transition metal nitrides

In the everlasting race for higher efficiency and machining speed in metal cutting industry, the ratio of tool cost to total machine cost has steadily increased. This fuels the modern quest for hard coatings which can resist contact temperatures exceeding 1000°C and the chemical and abrasive wear that come hand in hand with it [1-3]. Most prominent are transition metal nitrides (TMNS), which, depending on the particular constituents, show beneficial functional properties to owe to their ionic, covalent and/or metallic bonding [4]. Typical examples for binary TMNs are CrN and TiN, which crystallize in the cubic B1 structure and show moderate hardness of ~20 GPa and limited oxidation resistance up to 650 and 550°C, respectively [5]. Replacing of Ti and Cr atoms in TMNs with Al leads to both a significant increase in hardness and oxidation resistance [2].

Synthesis of AlCrN coatings has been pioneered at the turn of the millennium [6-7] leading to increased scientific interest on this ternary TMN. It has been proven since, that the addition of Al enhances the hardness, oxidation resistance and wear resistance of previously established CrN coatings by formation of a face centred cubic metastable solid solution (c-)  $Al_xCr_{1-x}N$ . However, when the chemical composition exceeds an Al content of  $x \sim 0.7$ , the hexagonal wurtzite (w-) Al(Cr)N B4 structure is formed [8]. Generally, the c-AlCrN exhibits a higher hardness [9], whereas the w-Al(Cr)N has an advantageous decomposition route (Fig. 1), by delaying the formation of  $Cr_2N$  and further metallic Cr accompanied by release of  $N_2$ . This last decomposition step is considered to be detrimental to the coating performance [10].

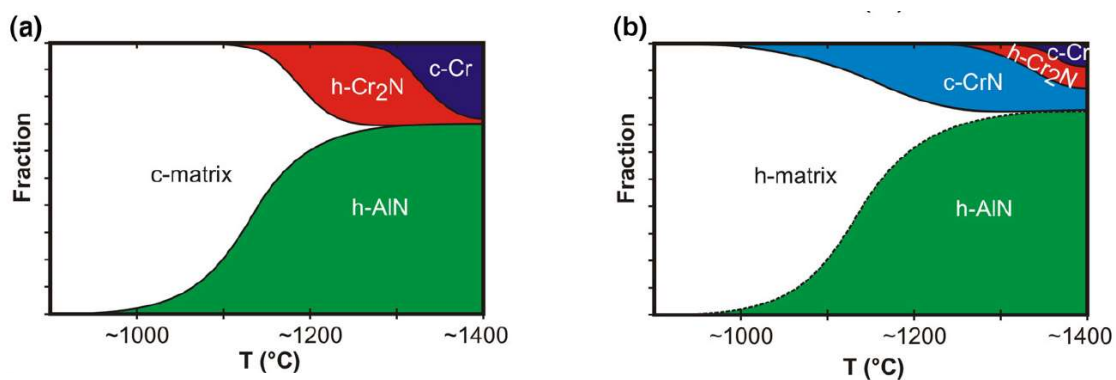


**Figure 1:** Phase development of fcc AlCrN (a) and w-Al(Cr)N as a function of annealing temperature [10].

In the case of c-AlCrN, decomposition of the metastable solid solution starts at  $\sim 1000^{\circ}\text{C}$  with the precipitation of w-AlN at the grain boundaries and the concluding enrichment of Cr in the remaining matrix as shown in Fig. 1a. The low stability of the CrN bonds leads to N-loss and the formation of h-Cr<sub>2</sub>N and N<sub>2</sub> and finally c-Cr [10]. Meindlhumer *et al.* [11] used the recently developed in situ high temperature high-energy grazing incidence transmission X-ray diffraction (HT-HE-GIT XRD) to investigate the complete decomposition pathway of c-AlCrN. The experiment revealed a significant lower onset of decomposition at  $\sim 700^{\circ}\text{C}$ , which limits the application of these c-AlCrN coatings to temperatures of up to  $800^{\circ}\text{C}$ . Furthermore, the phase transformations at different temperatures were correlated to similar stress energy thresholds.

The route of decomposition of the w-Al(Cr)N phase is less explored compared to c-AlCrN. Due to the already predominant wurtzite phase, w-Al(Cr)N is considered to be more favourable for service at high temperatures. The decomposition starts with the precipitation of c-CrN which reduces the Cr-content in the remaining matrix (Fig. 1b). The CrN precipitates are enclosed in an w-AlN matrix, which delays the further decomposition into h-Cr<sub>2</sub>N and N<sub>2</sub> [10] making it a promising candidate for grain boundary segregation engineering.



## Grain Boundary Segregation Engineering

In order to understand the further discussion, one has to step back and take a look at the topic of grain boundary segregation engineering. Generally, grain boundaries can be considered as twofold blades in materials' design. On one hand they can pose as its critical weakness if effects such as inter-crystalline fracture and stress corrosion cracking are pronounced, especially in brittle ceramics. On the other hand, as described by the Hall-Petch model, both materials' hardness and toughness are increased as a result of the decreasing size of crystalline grains (and simultaneous increasing the density of the grain boundaries), which bind the movement of dislocations [12].

The field of grain boundary segregation engineering seeks to solve elements of low miscibility in a poly-crystalline matrix and successively induce a segregation by applying a suitable heat treatment [13-15]. The segregation of the elements at the grain boundaries should then lead to a combined increase of yield strength and ductility. In the case of a Fe-8wt.% Mn alloy, increased ductility was achieved via a 48h heat-treatment at a temperature of 600°C. The heat treatment led to the formation of a Mn-rich austenite phase at the martensite interlath boundaries providing ductility while maintaining high yield stress required for this alloy [14].

The Achilles heel of TMN coatings is their susceptibility to brittle intercrystalline failure. The motivation of grain boundary segregation engineering in TMNs is to increase toughness of these coatings via blocking the fracture path at the underdense grain boundaries using dedicated segregation of secondary phases. However, mostly extrinsic toughening mechanisms are used nowadays in advanced TMN coatings [16], such as multi-layered microstructure based on materials of highly different Young's modules [17] or sculptured columnar grains [18] or even combinations of both [19]. Therefore, a material with even further increased thermal stability compared to w-AlCrN has to be found to serve as an additional toughening element. Recent works by Jäger *et al.* [20] showed superior thermal stability AlCrSi<sub>x</sub>N coatings compared to conventional c-AlCrN. It was shown that the addition of Si leads to the formation of a nanocomposite with AlCrN grains encapsulated in an amorphous Si<sub>x</sub>N<sub>y</sub> matrix. This hinders diffusion, thus preventing the decomposition of CrN and the formation of secondary phases at the grain boundaries.

Modern coatings seek to utilize these microstructural designs' concepts and phase compositions in order to maximize properties as (i) thermal stability (ii) hardness or (iii) fracture toughness [20, 21]. This is the starting point for the present thesis.

## Thesis Objective

The aim of this thesis is evaluate the concept of grain boundary segregation engineering for AlCrN hard coatings, which were synthesized by cathodic arc evaporation and subsequently annealed. The main thesis goal is to identify coatings' microstructures, compositions and annealing conditions, which application result in the improvement of mechanical properties.

Therefore, in a first step towards this goal, a graded  $(\text{Al}_{0.8}\text{Cr}_{0.2})_{1-x}\text{Si}_x\text{N}$  coating with a varying Si content up to  $x=0.05$  will be deposited and investigated in regards to its microstructure and mechanical properties. Measurements will be taken in its as-deposited state as well as after different variants of a dedicated heat treatments in order to identify conditions resulting in the relevant segregation at grain boundaries. The microstructural and phase stability will be investigated by cross-sectional X-ray nanodiffraction (CSnanoXRD) in small-angle and wide-angle X-ray diffraction conditions (SAXD and WAXD) and scanning electron microscopy (SEM). Changes of hardness and indentation modulus over the coating cross-section and the influence of the heat treatment are monitored by cross-sectional nanoindentation.

From this investigation, two favourable compositions will be selected for the deposition of multilayered coatings. Those shall possess a multilayered microstructure, wherein the segregation of CrN to the grain boundaries forces transcrystalline fracture, while the small, non-segregating interlayers force the crack growth to switch to intercrystalline propagation. The two multilayered coatings with different interlayer thicknesses and the reference materials will be tested for their mechanical properties in as-deposited and heat-treated state and the mechanical properties will be correlated to their unique microstructure.

Here presented thesis shall indicate a new promising recipe to increase the fracture resistance of AlCrN coatings with predominantly wurtzite crystal structure.

This chapter provides an overview of the used instruments and evaluation methods for the experiments conducted in this diploma thesis. Further an in-depth focus is taken towards the accuracy of Young's modulus evaluation from micro-mechanical tests by considering the testing system compliance.

## Physical Vapour Deposition (PVD)

The AlCrN coatings were deposited by cathodic arc evaporation (Vacotec alpha 400P, Voestalpine-eifeler) using a target current of 100 A, a substrate bias voltage  $U_B = -100$  V, a nitrogen pressure  $p_{N_2} = 4$  Pa and a deposition temperature of  $T_S = 475^\circ\text{C}$ . The substrate carousel was rotated at a speed of 2 rpm and the target-to-substrate distance was approximately 100 mm. All samples were deposited on mirror-polished cemented carbide (WC, 10 wt.% Co) substrates of a dimension of  $10 \times 5 \times 5$  mm<sup>3</sup>. For better adhesion, a 300 nm TiN base layer was deposited beforehand. The whole inner chamber was plasma cleaned prior to deposition. The here mentioned conditions are valid for all depositions performed during this project.

As the aim of this thesis was to investigate the influence of Si on the segregation of secondary phases at the grain boundaries, an  $\text{Al}_{0.8}\text{Cr}_{0.2}\text{N}$  coating with a Si gradient deposited. The Si-gradient was introduced at a projected coating thickness of 1.8  $\mu\text{m}$ , by gradually changing the composition of the process gas from pure  $\text{N}_2$  to a mixture of 97%  $\text{N}_2$  and 3%  $\text{SiH}_4$ .

By implementing the knowledge gained from CSnanoXRD (*cf.* Fig. 13-16), two multi-layered coatings were subsequently deposited for the final performance tests. The chosen target materials were strongly segregating  $\text{Al}_{0.8}\text{Cr}_{0.2}\text{N}$  and thermally stable  $(\text{Al}_{0.7}\text{Cr}_{0.3})_{0.9}\text{Si}_{0.1}\text{N}$  [20], with a presence of three cathodes each, in the deposition chamber. For reference measurements, two reference coatings consisting of the above two base materials were also deposited at the same conditions. The coatings architectures and compositions prepared by the PVD process are outlined in Table 1.

**Table 1:** An overview of the coatings investigated in this thesis with their labels and the target composition.

<i>Sample Name</i>	<i>Coating Design and Target Composition</i>
GBS-Si <sub>x</sub>	7 μm (Al <sub>0,8</sub> Cr <sub>0,2</sub> ) <sub>1-x</sub> Si <sub>x</sub> N
GBS-Si <sub>0</sub>	4 μm Al <sub>0,8</sub> Cr <sub>0,2</sub> N (reference)
GBS-Si <sub>10</sub>	4 μm (Al <sub>0,7</sub> Cr <sub>0,3</sub> ) <sub>0,9</sub> Si <sub>0,1</sub> N (reference)
GBS-Ml <sub>1</sub>	12× (50 nm (Al <sub>0,7</sub> Cr <sub>0,3</sub> ) <sub>0,9</sub> Si <sub>0,1</sub> N - 500 nm Al <sub>0,8</sub> Cr <sub>0,2</sub> N)
GBS-Ml <sub>2</sub>	12× (50 nm (Al <sub>0,7</sub> Cr <sub>0,3</sub> ) <sub>0,9</sub> Si <sub>0,1</sub> N - 250 nm Al <sub>0,8</sub> Cr <sub>0,2</sub> N)

## Heat Treatment

The energy barrier for the segregation of Si to the boundaries of columnar grains and also interlayers boundaries was overcome by a heat treatment in a vacuum furnace at a base pressure of 2 Pa and heating/cooling rates of 0.5°K/s. The right amount of segregation was assessed by comparing the results of CSnanoXRD (Fig. 13-16) and SEM (Fig. 9-12) of the gradient sample GBS-Si<sub>x</sub> annealed at 1000, 1050 and 1100°C for 5 minutes each. Therefore, a peak heating temperature of 1050°C was selected as an optimum for this thesis objective.

## Focused Ion Beam machining (FIB)

Cross-sections of the gradient samples in as-deposited and annealed states were fabricated by focused ion beam (1540XB Crossbeam, Zeiss) operated at an accelerating voltage of 30 kV. First, a W protection layer was deposited onto the sample surface using the gas injection system of the FIB to inhibit damage of the surface by Ga<sup>+</sup>-ions and milling artefacts induced by the roughness of the sample surface. Afterwards the surface of the coating was polished using constantly decreasing currents in the range of 500 to 20 pA.

## Scanning Electron Microscopy (SEM)

Cross-sectional imaging was done in a SEM (LEO 1525, Zeiss) with 3 kV acceleration voltage and an aperture of 20  $\mu\text{m}$ . Furthermore, electron-dispersive X-ray spectroscopy (EDS, Quantax XFlash 6|60, Bruker) was performed in the above mentioned SEM. For this method, an acceleration voltage of 10 kV and an aperture of 60  $\mu\text{m}$  were applied.

## Cross-sectional X-ray nanodiffraction (CSnanoXRD)

CSnanoXRD was performed as proposed by Keckes *et al.* in 2012 [22] at the synchrotron source DESY (Deutsches Elektronen Synchrotron, Helmholtz Zentrum Geesthacht) at the P03 MINAXS beamline. Multi-layer Laue lenses [23] were used to focus an X-ray beam with a photon energy of 15 keV to a diameter of  $\sim 200$  nm.

At first, the substrate-coating interface was oriented parallel to the incoming X-ray beam by a set of absorption scans. For this purpose, the samples were rotated around the y axis (Fig. 2) and the absorption was measured in transmission using a silicon diode detector. The optimal sample orientation was determined by maximizing the absorption contrast between the WC-Co substrate and the coating.

Line scans across as-deposited and annealed samples were applied with a step size of 100 nm along the z-axis in WAXS and SAXS geometry (Fig. 2). At sample-detector distances of 198.639 and 1291.32 mm, a detector (Eiger2 X 9M, Dectris) was positioned in order to collect two-dimensional (2D) diffraction patterns in respective WAXD and SAXD geometries. The exact detector geometry was determined by a calibration using NIST corundum and NIST silver behenate powder for WAXD and SAXD geometries, respectively.

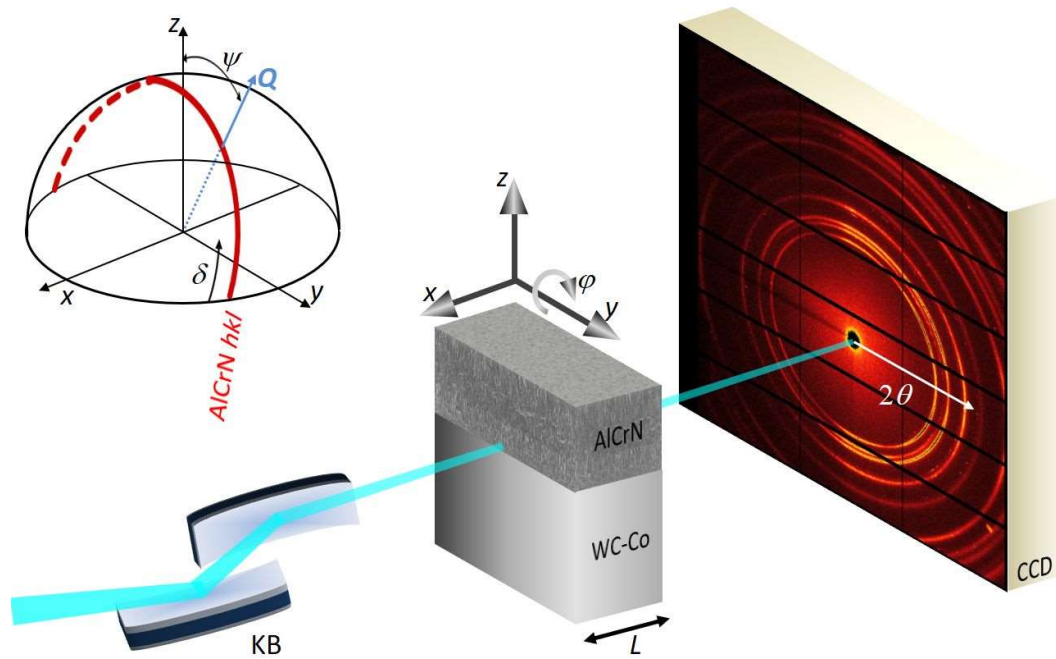


**Figure 2:** A schematic setup of the CSnanoXRD experiment performed on an exemplary AlCrN coating on WC-Co substrate in transmission WAXD geometry. The cross-sectional lamella with a thickness of  $L=50\ \mu\text{m}$  was scanned using a beam of  $\sim 200\ \text{nm}$  in diameter focused by a pair of Kirkpatrick-Baez mirrors [22]. The Debye-Scherrer rings were collected by a two dimensional detector - a charge-coupled device (CCD). Every ring position represents a diffraction on AlCrN ( $hkl$ ) crystallographic planes, which normals are parallel to the diffraction vector  $Q$ . The  $hkl$  Debye-Scherrer rings are projected on the stereographic projection top-left.

Analysis of the recorded Debye Scherrer rings was performed utilizing the software package PyFAI [24][25]. In a first step, the 2D patterns were azimuthally integrated in order to obtain phase plots. Furthermore, the software package was used to (i) qualitatively interpret the texture of the w-AlN 100 Debye-Scherrer rings, (ii) interpret the microstructure development by analysing full width at half maxima (FWHMs) and (iii) to correlate the ellipticity of the Debye Scherrer rings to elastic strains, which can furthermore be correlated to residual stresses of the 1<sup>st</sup> order in the samples, which all will be explained in detail in the following sections. The used parameters for stress evaluation were the X-ray elastic constant with  $\frac{1}{2}S_2 = 0.3903 \cdot 10^{-5}$  and Poisson's ratio  $\nu = 0.243$  for AlN 100.

### Condition of constructive interference

Bragg's law describes the constructive interference of electromagnetic waves on a crystal lattice. As indicated in Fig. 3, the waves of incident and scattered photons can be described by the primary and secondary wave-vectors  $K_0$  and  $K_1$ , respectively. If the difference in the path length between the primary and secondary waves diffracted on two neighbouring crystallographic planes of the lattice spacing  $d$  is an integer multiple of the wavelength  $\lambda$ , the diffracted photons are in phase. Therefore, the constructive interference results in the appearance of a diffraction maximum at the Bragg's angle  $2\theta$ , as indicated by the Bragg's law Eq. 1 [26].

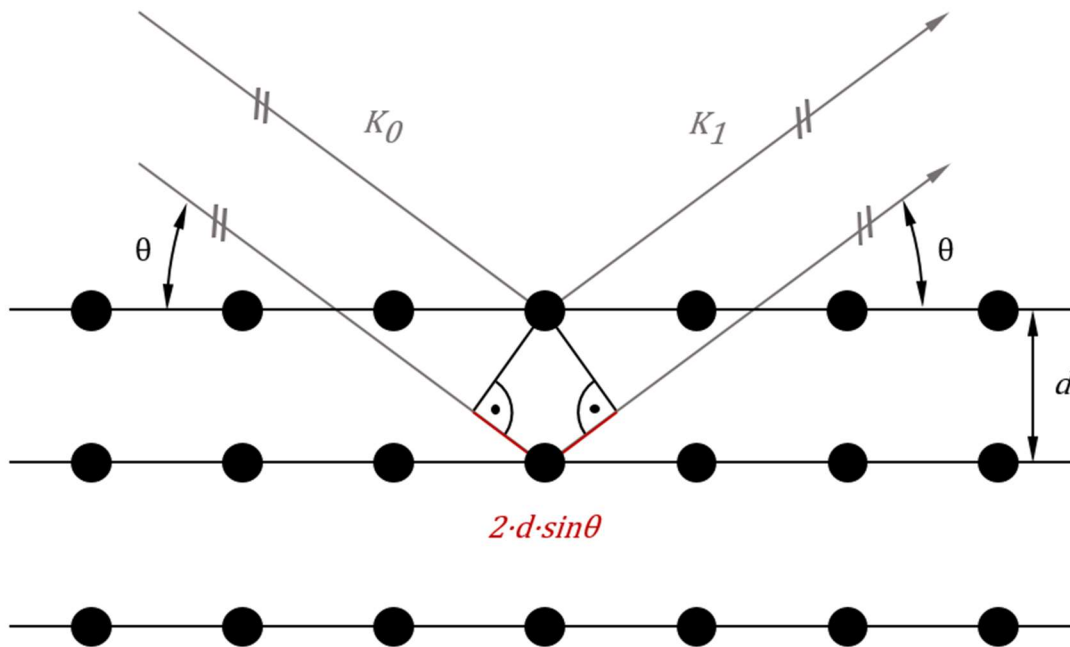


**Figure 3:** A visual display of the Bragg condition of constructive interference on a primitive cubic lattice.

Bragg's law, visualized by Fig. 3 can then be expressed as follows

$$2 \cdot d \cdot \sin \theta = n \cdot \lambda. \quad (1)$$

These points of constructive interference turn into Debye-Scherrer rings (Fig. 2) if the incident X-ray beam is monochromatic, the sample is polycrystalline without significant texture and the data are recorded by a 2D detector (cf. Fig. 2).



## *Determination of phase and family of lattice*

As previously mentioned every family of planes of a crystalline phase shows constructive interference at a specific Bragg angle  $\theta$ . Therefore, CSnanoXRD is particularly useful for identifying phases and phase transformations, which is usually done in an intensity  $I$  vs  $2\theta$  plot. This plot is generated by integrating the 2D detector images azimuthally and comparing the diffractogram to reference diffractogram provided by the Powder Diffraction Files (PDF) Database (International Centre for Diffraction Data, ICDD) [27, 28].

## *Analysis of Peak Broadening*

If an ideal parallel and monochromatic X-ray is diffracted by a single coherently diffracting domain of infinite thickness, all diffraction peaks should appear perfectly sharp. This concludes that the peak width, per convention measured as FWHMs or integral breadth  $\beta$  can be attributed to an abundance of properties such as (i) size of coherently diffracting domains  $D$ , (ii) gradients of strains of 1<sup>st</sup> order within the X-ray gauge volume and (iii) strains of the 2<sup>nd</sup> and 3<sup>rd</sup> order, in general caused by lattice defects. Nevertheless, the Scherrer equation (Eq. 2) established itself as a useful tool in estimating the size of  $D$  [26]. The parameter  $K$  is a dimensionless factor close to unity and is chosen to differentiate between equiaxed and elongated grains. The crystallite size analysis should however, always be accompanied by other methods such as SEM in order to draw relevant conclusions. The Scherrer equation giving a relationship between the size of coherently diffracting domains is denoted as follows:

$$D = \frac{K \cdot \lambda}{\beta \cdot \cos \theta} \quad (2)$$

In this thesis the used 2D data was integrated for each section of an azimuthal range of  $\frac{360^\circ}{n}$ , further labelled as cakes.

## Small Angle X-ray Scattering (SAXS)

Braggs Law indicates that the periodic length of the diffracting domain  $D$  and the angle of diffraction  $\theta$  are inversely proportional. Therefore, long range variations of electron density, such as (i) grain boundaries (ii) cracks and pores or (iii) interfaces show reflections at small angles in the range of  $0.1^\circ$  to  $10^\circ$ , depending on the beam energy.

In this thesis, the complex sputter kinetics of the arc-evaporation together with the rotation of the substrate carousel leads to a variation of elemental composition across the deposited coatings. In following, these periodic elemental variations also lead to small-angle X-ray diffraction signal from which the layer periodicity and its thermal stability can be estimated. For the quantitative evaluation of the layer periodicity, Bragg's law is applied (*cf.* Eq. 1).

## Evaluation of residual stresses

Strains and stresses of the 1<sup>st</sup> order result in the directionally uniform changes of the crystal lattice spacing and are henceforth denoted as macro strains  $\varepsilon_{ij}^{hkl}(z)$  and stresses  $\sigma_{ij}(z)$ . From CSnanoXRD, both properties can be evaluated for each individual phase and, in the case of strains, also for the family of planes. For an isotropic material, the relationship between macro strain and stress can be expressed by Eq. 3, wherein  $\frac{1}{2}S_2^{hkl} = \frac{1+\nu^{hk}}{E^{hkl}}$  and  $S_1^{hkl} = \frac{\nu^{hkl}}{E^{hkl}}$  are  $hkl$ -dependent X-ray elastic constants (XEC), which have to be determined by using a particular grain interaction models [29].

$$\varepsilon_{ij}^{hkl}(z) = \frac{1}{2}S_2^{hkl}\sigma_{ij}(z) + \delta_{ij}S_1^{hkl}\sum_k\sigma_{kk}(z) \quad (3)$$

Furthermore, the unknown strain in the sample  $\varepsilon_{ij}^{hkl}(z)$  can be related to the orientation dependent lattice strain  $\varepsilon_{\delta\theta}^{hkl}(z)$  by Eq. 5, which in turn can be expressed as the deviation of the orientation dependent lattice spacing  $d_{\delta\theta}(z)$  from the lattice spacing of the respective family of planes at thermal equilibrium  $d_0$ :

$$\varepsilon_{\delta\theta}^{hkl}(z) = \frac{d_{\delta\theta}(z) - d_0^{hkl}}{d_0^{hkl}}. \quad (4)$$

$$\varepsilon_{\delta\theta}^{hkl}(z) = \sin^2\theta\varepsilon_{11}^{hkl}(z) + \cos^2\theta\sin^2\delta\varepsilon_{22}^{hkl}(z) + \cos^2\theta\cos^2\delta\varepsilon_{33}^{hkl}(z) \quad (5)$$

By a substitution of the macro strains in Eq. 5 for macro stresses from Eq. 3, Eq. 6 is constructed. Additionally, in a coating without applied external loads, the assumption of equibiaxial stress state is valid. Therefore, all shear components of  $\sigma_{ij}$  ( $i \neq j$ ) and out of plane normal stress component  $\sigma_{33}(z)$  are considered zero and the remaining in plane stress components  $\sigma_{11}(z)$  and  $\sigma_{22}(z)$  are considered equal. The result is expressed in Eq.6. [30]

$$\begin{aligned} \frac{d_{\delta\theta} - d_0^{hkl}}{d_0^{hkl}} = & \sigma_{11}(z) \left[ \frac{1}{2} S_2^{hkl} \sin^2 \theta + S_1^{hkl} \right] \\ & + \sigma_{22}(z) \left[ \frac{1}{2} S_2^{hkl} \cos^2 \theta \sin^2 \delta + S_1^{hkl} \right]. \end{aligned} \quad (6)$$

As the expression of the derivative  $\frac{\partial d_{\delta}(z)}{\partial \sin^2 \delta}$  is formed in Eq. 7, a linear correlation to the macro strain  $\sigma_{22}(z)$  can be expressed as follows [30]:

$$\frac{\partial d_{\delta}(z)}{\partial \sin^2 \delta} = \sigma_{22}(z) \cdot \frac{1}{2} S_2^{hkl} d_0^{hkl} \cos^2 2\theta \quad (7)$$

## Cross Sectional Nanoindentation

In order to prepare the samples' cross-sections for nanoindentation, multiple polishing steps were carried out. The previously mirror polished samples were milled in an Ion Milling System (E-3500, Hitachi) at an acceleration voltage of 6 kV and a discharge voltage of 4 kV for 5 hours. Finally, the final surface roughness was improved using a FIB in a dual beam FIB-SEM "LEO 1540XB, Zeiss" operated at 30 kV accelerating voltage applying constantly decreasing currents down to 500 pA.

Nanoindentation testing was performed using a Hysitron TS 77 Select nanoindenter and a cube corner tip provided by Synton-MDP LTD. The tip was calibrated on a sample of fused silica, which was provided for this purpose by the manufacturer. The resulting tip function was verified for an indentation depth range from 20-500 nm.

The maximum force  $P_{max}$  was chosen to be 1000  $\mu\text{N}$  and was applied at a loading/unloading rate of 200  $\mu\text{N/s}$ . In between those steps the maximum load was held for 2 s. An indentation modulus and hardness mapping was performed in arrays of  $10 \times 4$  indents with a distance of 1  $\mu\text{m}$  between the indents (Fig. 4).

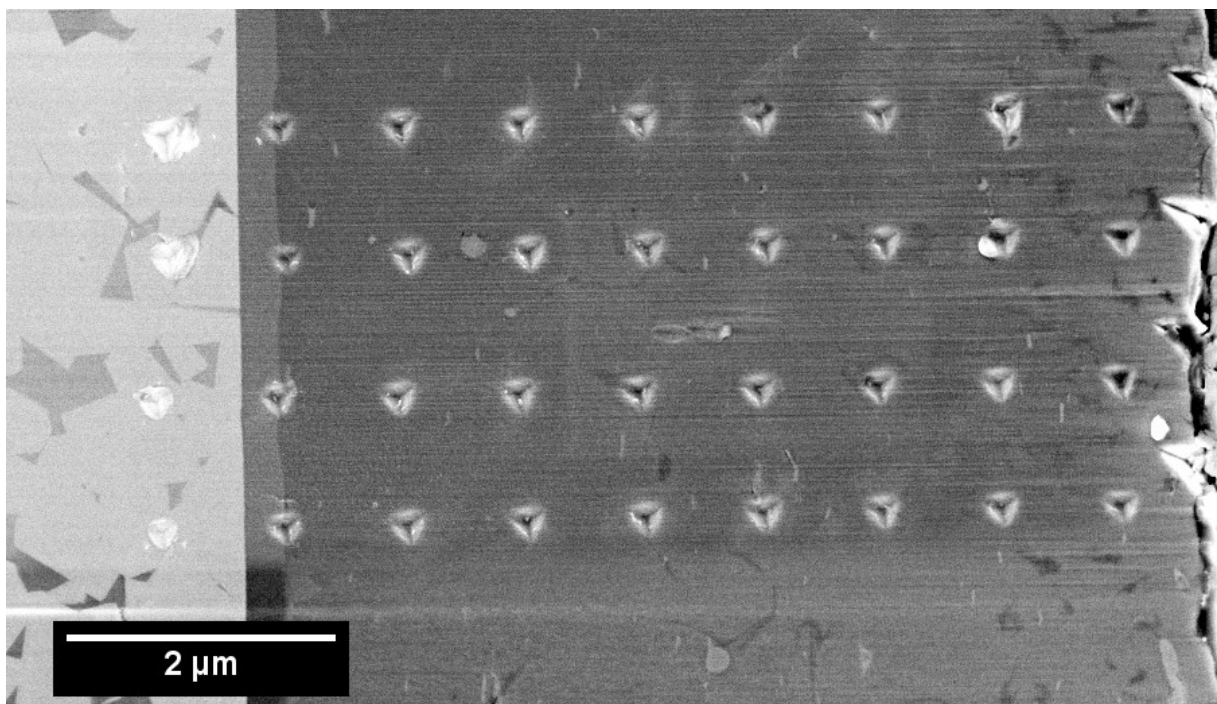


**Figure 4:** An exemplary array of indents on an  $(\text{Al}_{0.8}\text{Cr}_{0.2})_{1-x}\text{Si}_x\text{N}$  coating cross-section. The indents range from the WC-Co substrate across the TiN bonding layer throughout the coating.

## Evaluation of Nanoindentation Data by the Method of Oliver and Pharr

Foundations of nanoindentation were laid down by Oliver and Pharr in 1992 [31]. At first the contact depth was defined according to Eq. 8 using the depth at zero load  $h_0$  and the depth at maximum load  $h_{max}$ . From there on the coating's hardness  $H$  and elastic modulus  $E_f$  were derived using Eq. 9-11 considering the slope of the unloading curve  $S$  at the point of maximum load  $P_{max}$  [32-33].

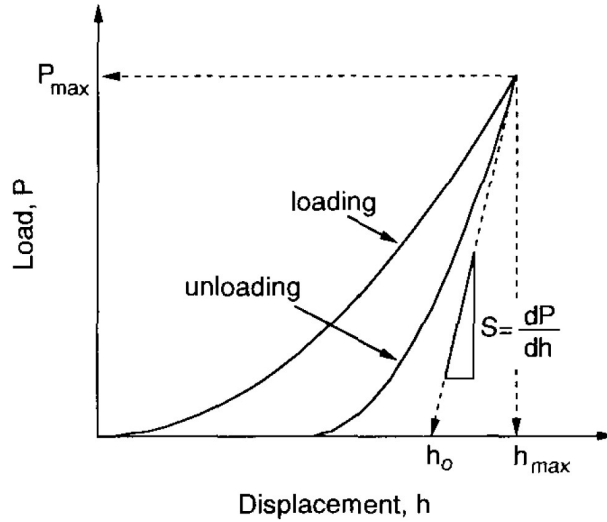


Figure 5: The schematic load-displacement curve for the nanoindentation experiment [32].

$$h_c = h_0 + 0.25 (h_{max} - h_0) \quad (8)$$

$$H = \frac{P_{max}}{A_c(h_c)} \quad (9)$$

$$S = \frac{dP}{dh} = \frac{2}{\sqrt{\pi}} E_r \sqrt{A_c(h_c)} \quad (10)$$

$$\frac{1}{E_r} = \frac{(1 - \nu^2)}{E_f} + \frac{(1 - \nu^2)}{E_i} \quad (11)$$

A correct application of the prior mentioned equation requires a detailed knowledge of the contact area as a function of contact depth, further named tip function  $A_c(h_c)$ . This function was determined using a material of known hardness and multiple indentations of different depth. Accordingly the tip function was approximated using Eq. 12 [32-33].

$$A(h_c) = 24.5 h_c^2 + C_1 h_c^{0.5} + C_3 h_c^{0.25} + C_4 h_c^{0.125} \quad (12)$$

## *In situ* Cantilever Bending

The assessment of Young's modulus, fracture stress and fracture toughness was conducted by *in situ* micromechanical testing of cantilever beam specimens. These were fabricated by a FIB workstation Auriga Crossbeam from Zeiss operating at an accelerating voltage of 30 kV. On each sample, 8 cantilevers were prepared, 4 unnotched ones for evaluating Young's modulus and fracture stress and 4 notched cantilevers to evaluate fracture toughness (Figs. 27-29). A rough milling for the removal of the surroundings of the cantilevers was performed with decreasing currents of 5 nA to 500 pA, while final polishing was done with a current of 100 pA. Finally, at the cantilevers dedicated for fracture toughness, a notched was milled using a current of 10 pA. The width  $B$  and thickness  $t$  were chosen to be 2 and 3  $\mu\text{m}$  respectively. The cantilever length  $L$  or distance to the point of load was set to 10  $\mu\text{m}$  and 13  $\mu\text{m}$  for notched and unnotched cantilevers, respectively.

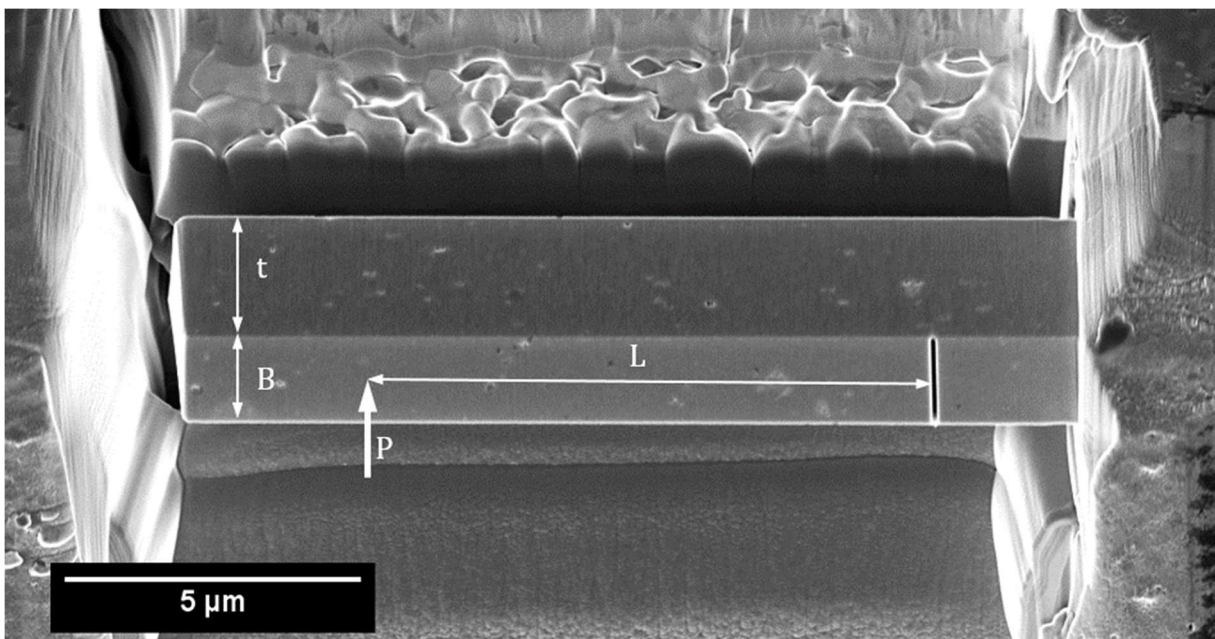


*Figure 6: A SEM image of a representative micro-cantilever prior to testing.*

Cantilever testing to fracture was performed inside a SEM LEO 982, Zeiss by applying the critical load  $P_{max}$  with a nanoindentation device (PicoIndenter 85, Bruker) and a mounted sphero-conical tip. The testing was done in displacement-controlled mode with a speed of 20 nm/s, resulting in a strain rate in the range of  $\sim 10^{-3} \text{ s}^{-1}$  at the constraint of the cantilever [34].

After the experiment, the fracture surface of all cantilevers was imaged using a SEM LEO 1525, Zeiss operated at an acceleration voltage of 2 kV in order to measure the initial crack length of

the notched cantilevers and to verify that no prior cracking or other defects possibly invalidating the fracture experiments.

### *Euler-Bernoulli Beam Theory*

The purpose of the Euler-Bernoulli Beam theory is to describe the elastic mechanical response of a beam subjected to lateral (bending) loads at low deflection. Therefore, it is considered to be the basis of evaluation for the cantilever bending experiments [31-32].

In an ideal measurement system (where the stiffness of the machine  $S_s = \infty$ , *i.e.* the compliance of the system  $C_s = 0$ ), Eq. 13 yields the Young's modulus  $E$ . It is expressed by the slope  $\frac{\Delta P}{\Delta w}$  of the load-displacement curve and the cantilever geometry as follows

$$E = \frac{4}{B} \cdot \frac{\Delta P}{\Delta w} \cdot \left(\frac{L}{t}\right)^3. \quad (13)$$

Furthermore, the fracture stress  $\sigma_F$  is calculated using Eq. 14 from the load at critical failure  $P_{max}$  of the cantilever:

$$\sigma_F = 6 \cdot \frac{P_{max}L}{Bt^2}. \quad (14)$$

### *Estimation of the system compliance*

In this thesis, the slope of the load-displacement curve was furthermore corrected for the system compliance  $C_s$ . The system of indenter tip and cantilever was estimated as a set of springs connected in series as follows:

$$C_m = C_c + C_s, \quad (15)$$

where  $C_m$  is the measured compliance corresponding to the inverse slope of the load-displacement curve  $\frac{\Delta h}{\Delta P}$ ,  $C_c$  is the known compliance of the cantilever with a given Young's modulus and the geometry and  $C_s$  is the compliance of the system. The latter was empirically derived using cantilevers of different sizes made of Si and W with a known crystallographic

direction and therefore known elastic modulus  $E_{th}$ . From this material property, the cantilever compliance  $C_c$  was calculated according to

$$C_c = \frac{4}{E_{th}} \cdot \left(\frac{t}{l}\right)^3. \quad (16)$$

$$C_m = \frac{\Delta h}{\Delta P} \quad (17)$$

In the plot of measured compliance  $C_m$  against theoretical cantilever  $C_c$ , the intersection with the abscissa would represent an infinitely stiff cantilever. Therefore, the remaining compliance can be solely attributed to the system  $C_s$ . Based on the data from multiple W and Si samples, such a plot was generated as seen in Fig 7 and the system compliance could be determined as  $C_s = 0.170 \frac{\text{nm}}{\mu\text{N}}$ .

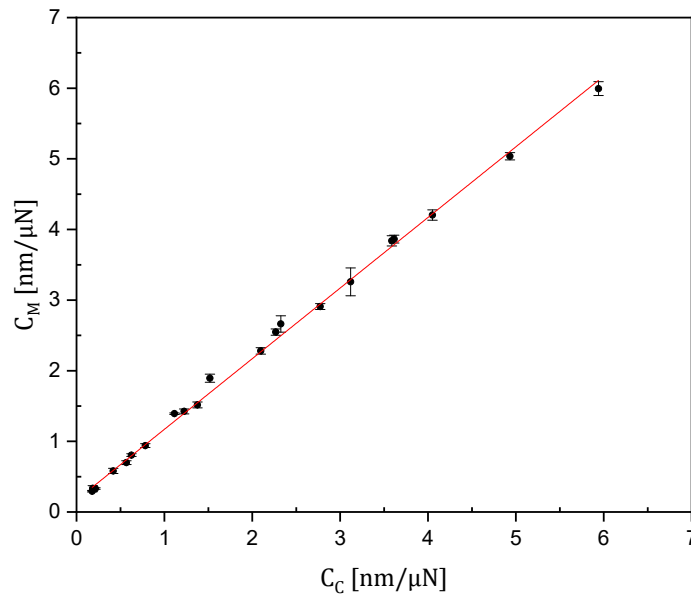


**Figure 7:** Measured compliance  $C_m$  as a function of the cantilever compliance  $C_c$ .

This information was used to correct the Young's modulus  $E$  of all cantilevers in the manner of Eq. 18.

$$E = \frac{4}{B} \left( \frac{\Delta h}{\Delta P} - 0.170 \frac{\text{nm}}{\mu\text{N}} \right)^{-1} \left( \frac{L}{t} \right)^3. \quad (18)$$



## *Linear elastic fracture mechanics*

Fracture toughness was derived using linear elastic fracture mechanics appropriate for ceramic coatings. Its application demands, that (i) the plain strain condition expressed is valid and (ii) the occurring plastic zone is significantly smaller than all characteristic lengths of the material as expressed in Eq. 19 [36]. Since the samples investigated within this thesis showed no plastic deformation at all, the yield stress  $\sigma_{ys}$  was substituted by the fracture stress  $\sigma_f$ . However, since the fracture stress is below the yield stress for all investigated samples, the criterions for the application of linear elastic fracture mechanics were strengthened. These criterions were verified for all tested cantilevers.

$$a, B, t > 2.5 \cdot \left( \frac{K_{IC}}{\sigma_{ys}} \right)^2 \quad (19)$$

Furthermore, this theory requires an initial crack, which has to be known in size  $a$  and which is infinitely sharp. This was archived by pre-notching the cantilevers and leaving a thin material bridge at both sides. This bridges crack under relatively low load and create the needed sharp crack, which can be measured afterwards.

With these criterions met, the fracture toughness  $K_{IC}$  was calculated using Eq.20, at which the necessary geometry factor  $Y$ , which is specific to the cantilever design, was used from Tada *et al.* [37].

$$K_{IC} = \sigma \sqrt{\pi a} \cdot Y \left( \frac{a}{t} \right) \quad (20)$$

$$Y \left( \frac{a}{w} \right) = \sqrt{\frac{2t}{\pi a} \tan \left( \frac{\pi a}{2t} \right)} \cdot \frac{0.923 + 0.199 \cdot (1 - \sin \left( \frac{\pi a}{2t} \right))^4}{\cos \left( \frac{\pi a}{2t} \right)} \quad (21)$$

### *Irwin crack length correction*

The Irwin crack length correction makes further efforts in order to estimate the initial crack length. Within this theory the initial crack length  $a$  is extended by the radius of the plastic zone  $r_p$  and further labelled effective crack length  $a_{eff}$  (Eq. 23). The radius of the plastic zone can be estimated using Eq. 22 [36].

$$r_p = \frac{1}{2\pi} \cdot \left( \frac{K_I}{\sigma_{ys}} \right)^2 \quad (22)$$

$$a_{eff} = a + r_p \quad (23)$$

## Electron Dispersive X-ray Spectroscopy

The gradient coating GBS-Si<sub>x</sub> was characterized in regards to its chemical composition in order to correlate the depth resolved mechanical properties to a Si content in a quantitative manner. In addition, the coating composition was compared to the cathode composition used in the deposition process.

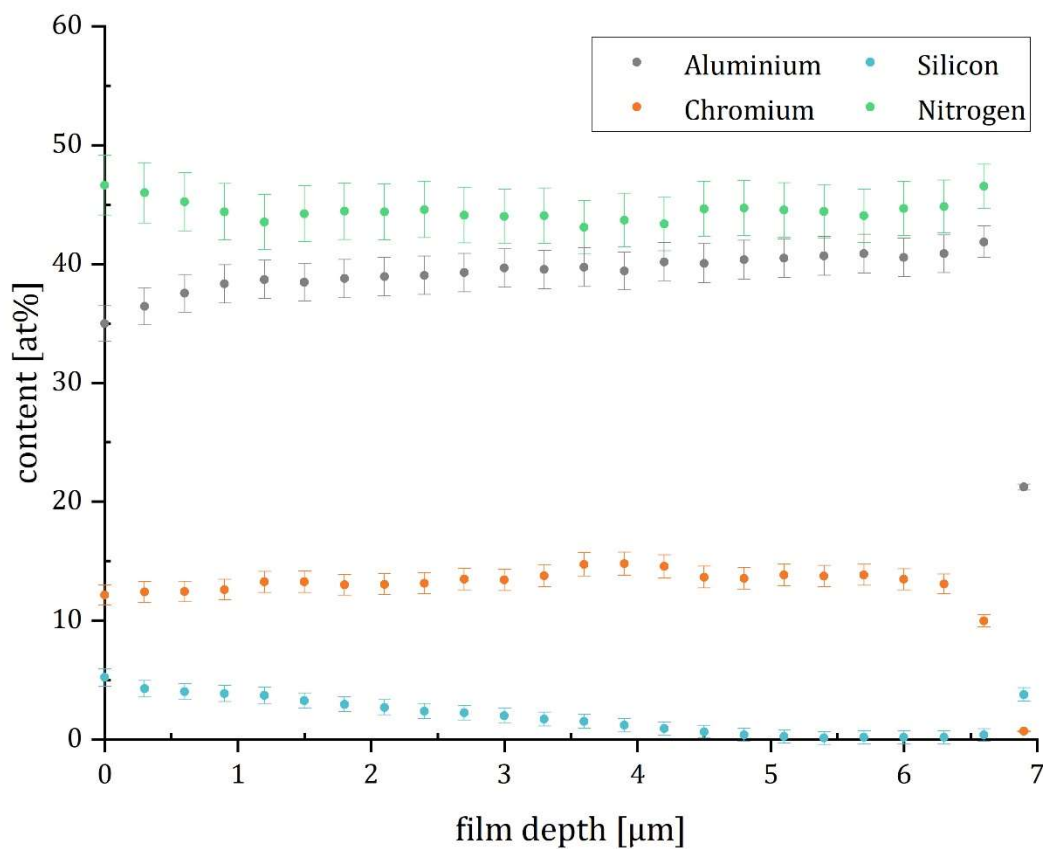


**Figure 8:** An EDX measurement of the GBS-Si<sub>x</sub> gradient coating in the as-deposited state, for relevant elemental composition.

EDX data from a representative GBS-Si<sub>x</sub> coating in Fig. 8 indicate a chemical composition gradient before the sample was exposed to various heat treatments in this work. Overall the coating shows a higher ratio of chromium than in the target composition of Al<sub>0.8</sub>Cr<sub>0.2</sub>N, which can be attributed to preferential sputtering. This means that it is statistically more probable for elements of less mass like Al to be sputtered away from the coating surface in favour of heavier elements like Cr [38]. Furthermore, an increase in the Si content can be seen from ~5 μm up to

the coating surface (Fig. 8). This trend together with the decreasing ratio of Al in the coating composition suggest that Si replaces Al within the lattice.

The ratio of N stays approximately constant over the whole sample composition (Fig. 8), indicating no change of N within the coating when applying a different gas mixture (*cf.* Methods).

## Cross-Sectional Microstructural SEM analysis

Cross-Sectional microstructural SEM analysis was performed complementary to the CSnanoXRD measurements in order to analyse the development of the microstructure as a function of the Si content as well as the particular heat treatments. Therefore, the conclusion drawn in the CSnanoXRD experiment could be interpreted correctly and *vice versa*.

### *Gradient coating GBS-Si<sub>x</sub> in as-deposited state*

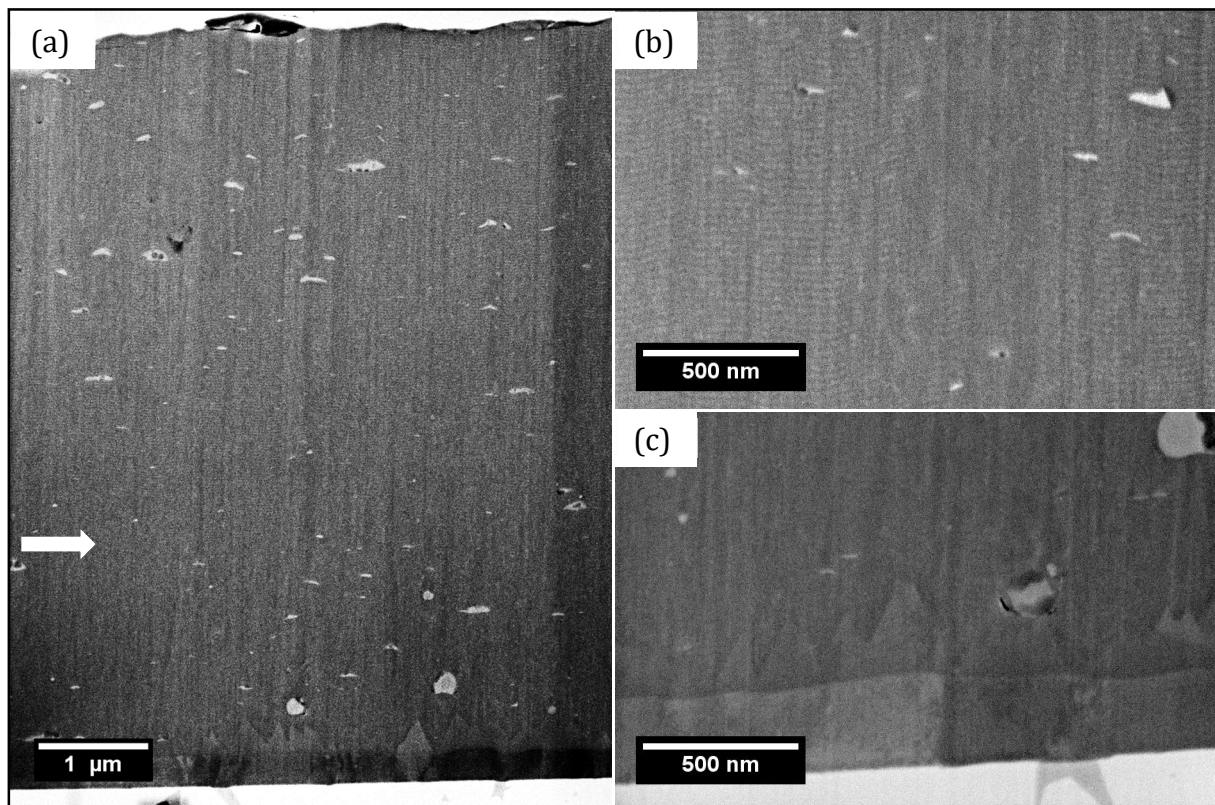


**Figure 9:** SEM-image of the GBS-Si<sub>x</sub> cross section in as-deposited state (a) shows layered microstructure. Further magnification reveals differences at the coating surface (b) and the coating-substrate interface (c).

An overview of the coating cross section is given in Fig. 9a, complemented with images of higher magnification of regions of interest at the substrate/coating interface (Fig. 9c) and close to the coating surface (Fig. 9b). A columnar grain growth was found for the TiN bonding layer and the bottom part of the Al<sub>0.8</sub>Cr<sub>0.2</sub>N coating. At the interface between the TiN base layer and the Al<sub>0.8</sub>Cr<sub>0.2</sub>N coating, large grains of pseudo-epitaxial grown c-Al<sub>0.8</sub>Cr<sub>0.2</sub>N on TiN are visible (Fig. 9c), which is later confirmed in the phase plot in Fig. 13. A nanolayered structure, is not visible in the Al<sub>0.8</sub>Cr<sub>0.2</sub>N, however it is verified by SAXD later in Fig. 17. This can be attributed to the low contrast provided by the rather small Al/Cr ratio shift. When starting the Si introduction

(indicated by the arrow in Fig. 9a), the columnar growth is interrupted and a nanocomposite layered microstructure is formed, as presented in Fig. 9c. Generally, all SEM images show droplets and pores of different sizes which are characteristic for cathodic arc evaporation, mainly because of the high deposition rate. In addition, Fig. 9b reveals a nanolayered microstructure which will be further investigated in Fig. 17 with SAXS.

### *Gradient coating GBS-Si<sub>x</sub> microstructure after annealing to 1000°C*

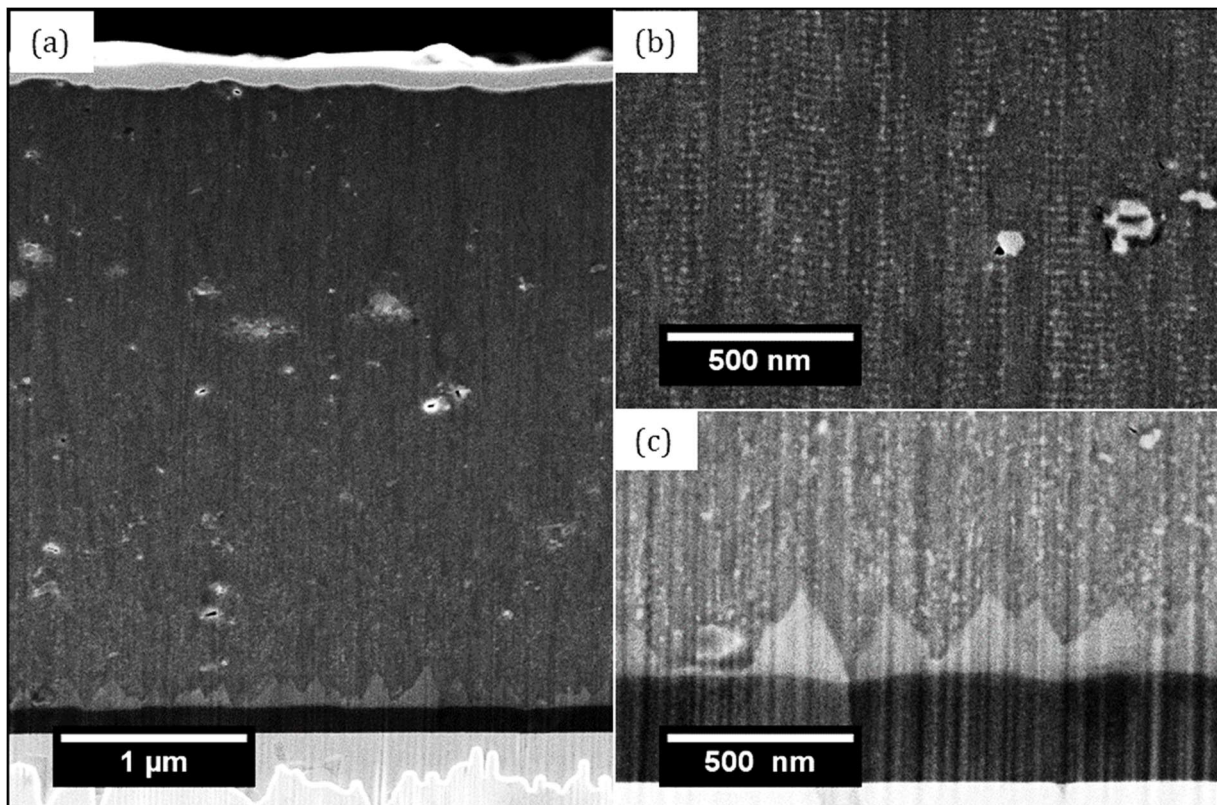


**Figure 10:** SEM-image of the GBS-Si<sub>x</sub>1000°C coating cross section (a) shows layered microstructure. Further magnification reveals differences at the coating surface (b) and the coating-substrate interface (c).

In Fig. 10a, at low resolution, no pronounced difference compared to the as-deposited coating can be observed. However, after a closer investigation at the substrate/coating interface and the coating surface, influences of the heat treatment are revealed (Fig. 10b,c).

At the interface of the TiN base sublayer and the coating, large grains of epitaxial growth are still similar to those in the as-deposited state. Contrary to the as-deposited coating, in the coating above precipitates have formed during the heat treatment, which according to the decomposition route (*cf.* Introduction) is most probably c-CrN (Fig. 10c). This statement is later

supported by the increased intensity of the 200 CrN reflections in the corresponding phase plot (Fig. 14a).

Right beneath the surface the observed nanolayered microstructure is still intact (Fig. 10b).

### *Gradient coating GBS-Si<sub>x</sub> microstructure after annealing to 1050°C*

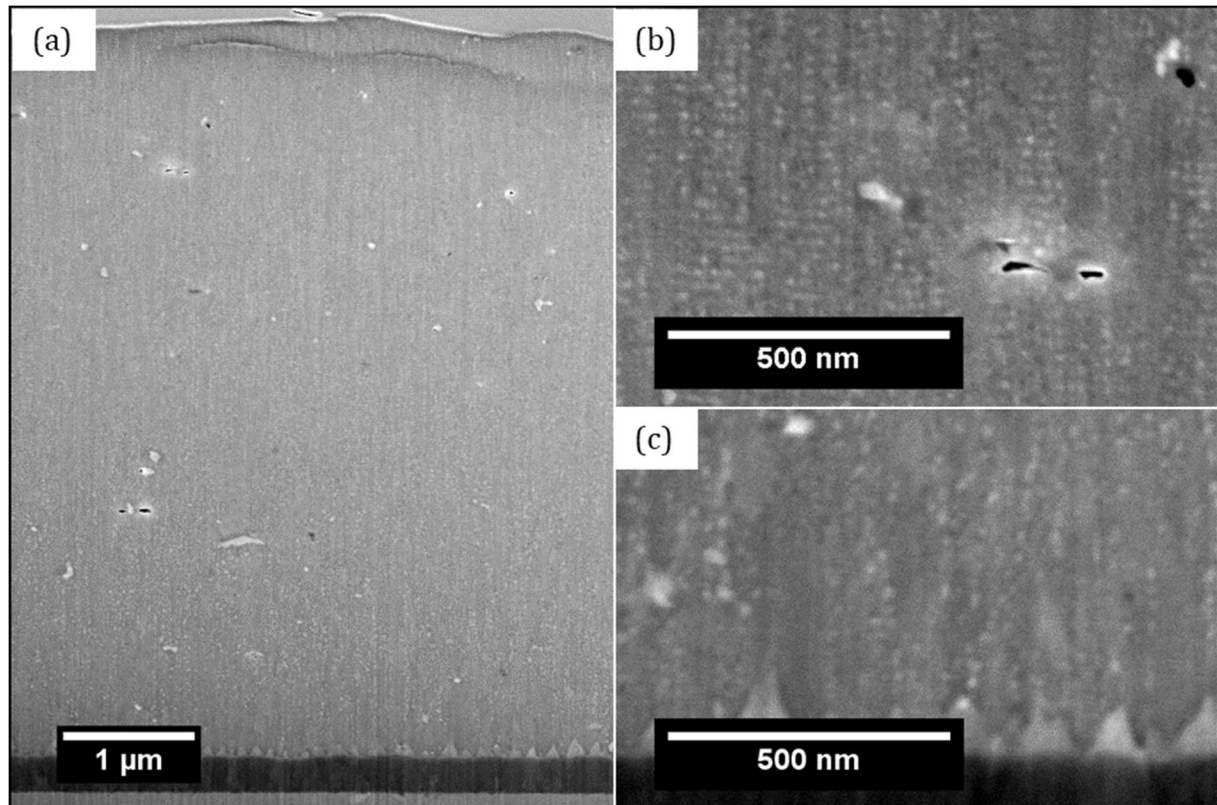


**Figure 11:** SEM-image of the GBS-Si<sub>x</sub>-1050°C coating cross section (a) shows layered microstructure. Further magnification reveals differences at the coating surface (b) and the coating substrate interface (c).

In Fig. 11a, again an overview of the cross section suggest an indifference of the coating to the thermal exposure, disproven after closer investigation (cf. Fig. 11b,c).

At the interface of the TiN base layer and the coating, the previously epitaxial c-AlCrN grains have been dissolved in the matrix of the coating (Fig. 11c). Furthermore, the precipitation of c-CrN is more pronounced than in the GBS-Si<sub>x</sub> 1000°C sample (cf. Fig. 10b).

In the upper part of the coating the nanolayers are still visible, but larger particles indicate a significant diffusion within these layers (Fig. 11b).

## Gradient coating GBS-Si<sub>x</sub> microstructure after annealing to 1100°C

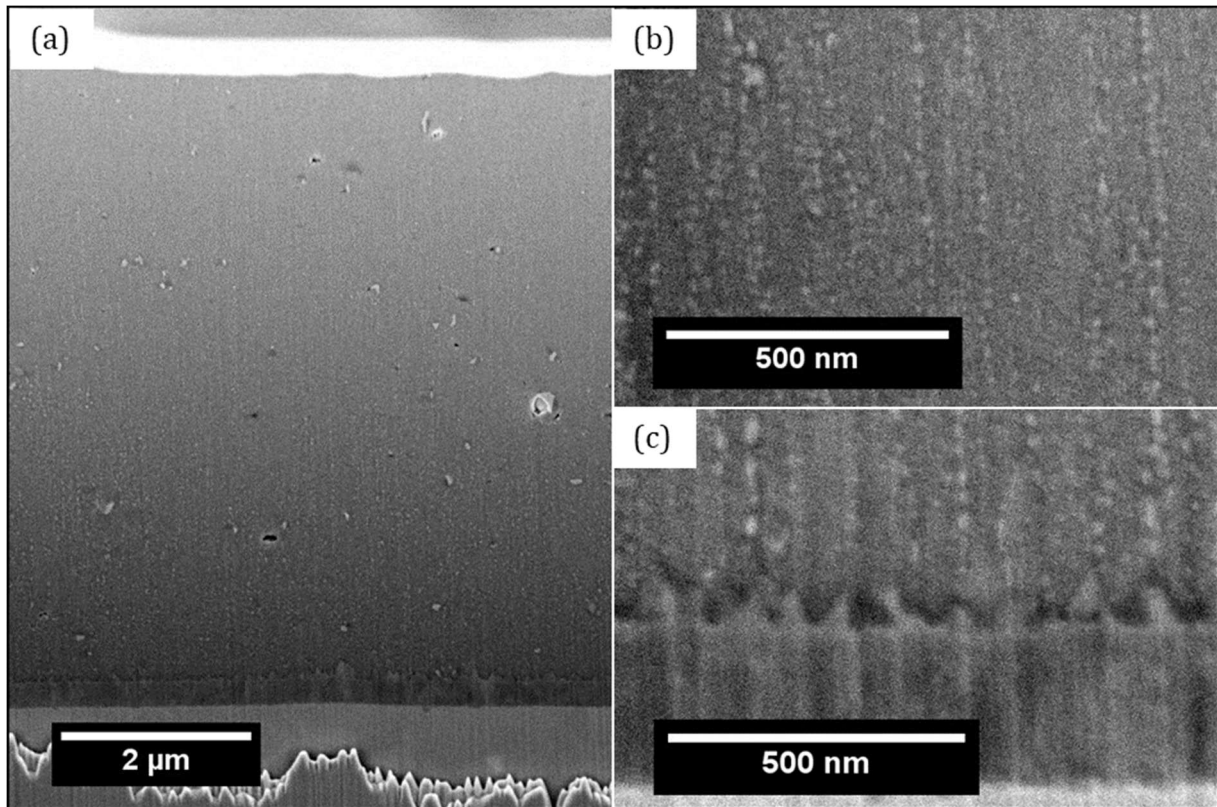


**Figure 12:** SEM-image of the GBS-Si<sub>x</sub>-1100°C coating cross section (a) shows layered microstructure. Further magnification reveals differences at the coating surface (b) and the coating-substrate interface (c).

Fig 12a, shows a clean cross-section of the heat treated coating. Structures visible in the substrate at the bottom part of the picture are remainders of the material removed by the FIB machining.

At the coating/substrate interface we can observe large precipitates (Fig 12c). Since no Cr<sub>2</sub>N reflection can be observed in the corresponding phase plot in Fig. 16, the precipitates can be attributed to c-CrN.

Furthermore, the conglomeration close to the surface of the coating has proceeded to a point, where only a discontinuous nanolayered structure can be seen (Fig 12b). From a microstructural point of view, the heat-treatment up to 1100°C leads to the precipitation within the coating regardless of the Si content and is therefore not suitable to induce composition dependent grain boundary segregation. However, this will be further proven by the CSnanoXRD data.



## Cross-Sectional X-ray Nanodiffraction – WAXS

CSnanoXRD in WAXS geometry was performed in order to characterize properties of crystalline phases within the coatings and specially to assess the precipitation of c-CrN after annealing at high temperatures, to analyse FWHM in regards to the grain structure and the development and relaxation of residual stresses.

### CSnanoXRD investigation of the graded GBS-Si<sub>x</sub> coating in as-deposited state

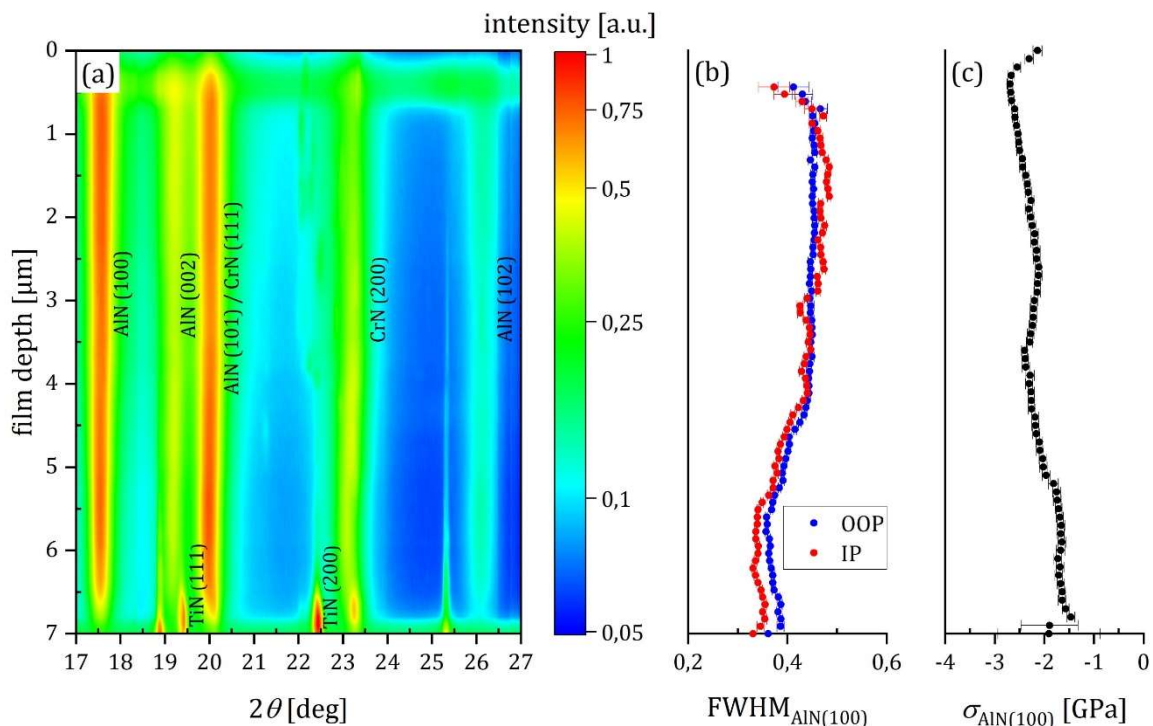


**Figure 13:** (a) A diffraction Intensity from GBS-Si<sub>x</sub> coating shows reflections of the wurtzite AlN and cubic CrN phases as well as reflection of the TiN bonding layer. Further analysis of the AlN (100) reflection reveals gradients in FWHM (b) and stress (c).

The phase plot in Fig. 13a indicates a presence of w-AlN and c-CrN phases in the coating (Fig 13a). Furthermore, at the coating depths below 5 μm, where the addition of Si begins, no additional phases were detected. Between the coating depths of 4.5 and 5.5 μm, an increasing FWHM as well as a change in the position of the CrN 200 reflection were revealed (Fig 13a,b). Additionally, a decreasing intensity of the CrN 200 reflection indicates an increased suppression of the formation of the cubic phase. It should be noted, that between the coating depth of 6.5 and 6.8 μm, no w-AlN phase was found indicating pseudo-epitaxial stabilization of Al<sub>0.8</sub>Cr<sub>0.2</sub>N

on TiN, which can be correlated to the large grains at the bottom of the coating (*cf.* SEM micrographs in Fig. 9).

A proceeding investigation of the AlN 100 Debye Scherrer ring shows an columnar grain microstructure with grains elongated in out of plane (OOP)-direction, which is indicated by the margin between the FWHM in OOP- and in plane (IP)-directions, respectively, at coating depths between 6.5 and 5  $\mu\text{m}$  (Fig 13b). Supplementary, the overall decrease of the FWHM in this region indicates an increasing grain size, caused by competitive grain growth [39].

At the coating depths of 5.5 to 4.5  $\mu\text{m}$  the overall FWHM increases while the margin between OOP and IP FWHM decreases, corresponding to an equiaxed grain morphology. This is further accompanied by a total grain refinement as seen by the increase of the FWHM in the coating surface direction (Fig 13b).

The compressive residual stress in the coating starts at the interface at -1.46 GPa and steadily increases up to a maximum of -2.69 GPa. Moreover a rise in the inclination of the stress profile can be observed in the same coating range as the rise in the FWHM (Fig 13c).

### *CSnanoXRD investigation of the graded GBS-Si<sub>x</sub> coating annealed at 1000°C*

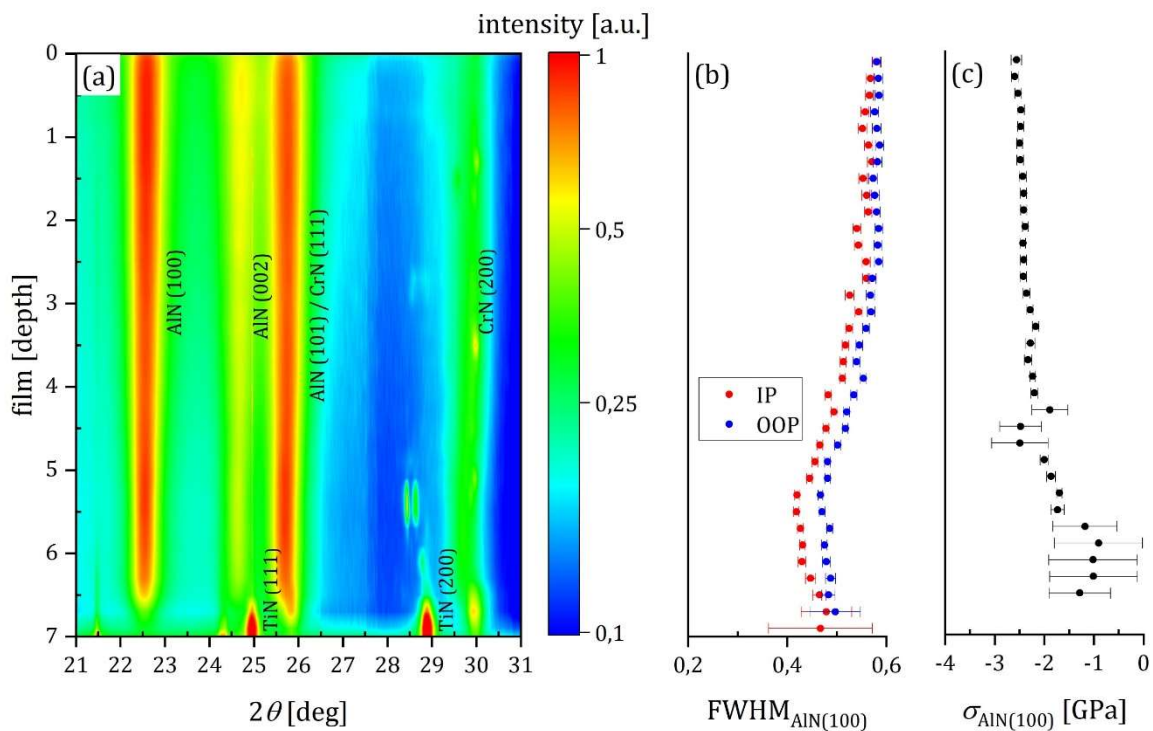


**Figure 14:** (a) Diffraction intensity distribution from GBS-Si<sub>x</sub> coating annealed at 1000°C shows maxima of the wurtzite AlN and cubic CrN phases as well as reflections from the TiN bonding layer at higher

coating depth. Further analyses of the AlN (100) reflection reveals influences of the heat treatment on the FWHM (b) and the stress (c).

The phase plot in Fig 14a suggests the perseverance of the w-Al(Cr)N and c-Cr(Al)N phases in the coating after the heat treatment up to 1000°C (Fig 14a). Between the coating depths of 4.5 and 5.5 μm, an increasing FWHM as well as a change in the position of the CrN 200 reflection are also still visible (Fig 14a,b). The same goes for the margin between 6.5 and 5 μm and the overall increase of the FWHM from the substrate coating interface to the coating surface (Fig 14b).

The compressive stress increases from -1.41 to -2.56 GPa within the thickness of the coating (Fig 14c). No relaxation of the compressive stress can be observed after this heat treatment, indicating no defect relaxation and significant change in microstructural features, despite the segregation of particles found in SEM.

### CSnanoXRD investigation of the graded GBS-Si<sub>x</sub> coating annealed at 1050°C

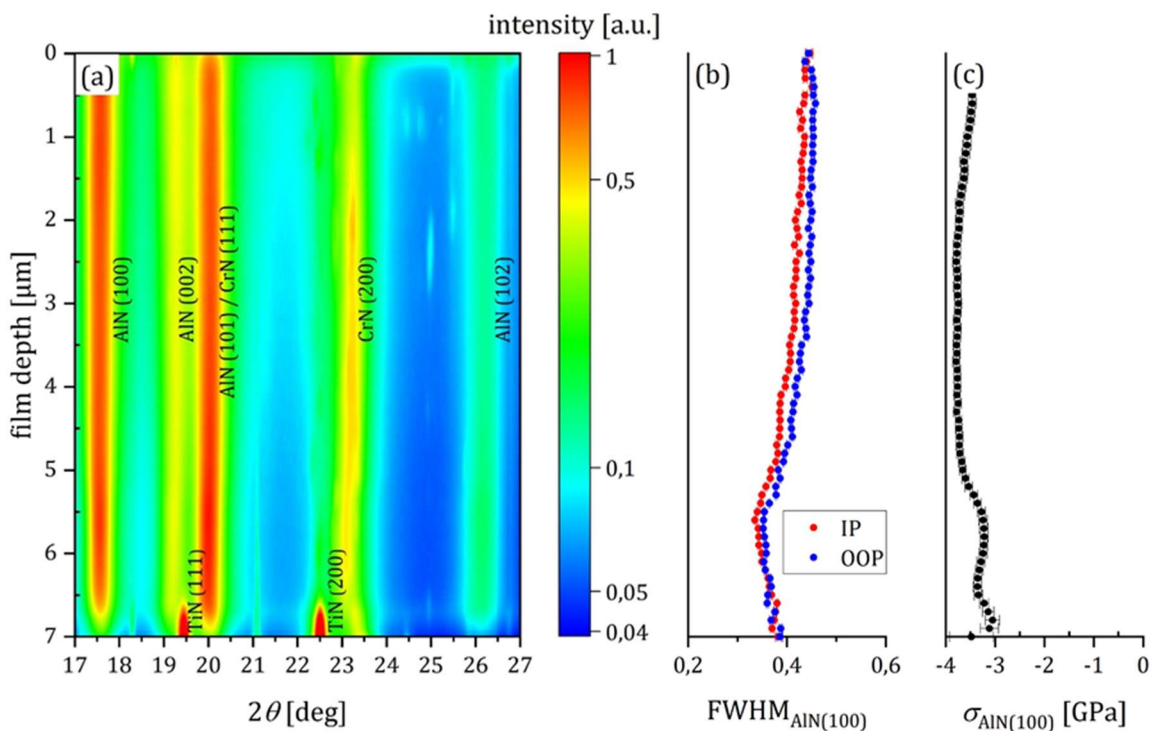


**Figure 15:** (a) Diffraction intensity distribution from the GBS-Si<sub>x</sub> coating annealed at 1050°C shows maxima of the wurtzite AlN and cubic CrN phases as well as reflections from the TiN bonding layer at higher coating depth. Further analyses of the AlN (100) reflections reveals an influence of the heat treatment on the FWHM (b) and the stress (c).

Again, the phase plot in Fig 15a suggests the perseverance of the w-Al(Cr)N and c-Cr(Al)N phases in the coating after the heat treatment up to 1050°C (Fig 15a). However, the c-AlCrN above the TiN base layer is nearly completely vanished, as suggested by the SEM data (*cf.* Fig. 11). Further visible is the positional shift of the CrN 200 reflection, which is less pronounced compared to the as-deposited state, and the increase of the FWHM between 5.5 and 4.5  $\mu\text{m}$  (Fig 15a,b).

A difference can be observed in the FWHM of the AlN 100 Debye Scherrer ring (Fig 15b), which is now of equal size in IP- and OOP-directions. Given the fact, that the grain morphology did not change much throughout the annealing (compare Figs. 9 and 11), it can be concluded that the secondary phase particles of CrN in the coating decrease the size of coherently diffracting domains and increase the FWHM in IP-direction (Fig 15b).

The compressive stress ranges from -3.17 to -3.77 GPa (Fig 15c) which is higher contrary to the other samples. This is related to the fact, that this coating was deposited on high-speed steel which has a different thermal expansion coefficient (TEC) than cemented carbide (*cf.* Discussion). Furthermore, a decrease of the compressive stress between the coating surface and 2  $\mu\text{m}$  coating depth can be observed, indicating a relaxation of the compressive stress (Fig 15c).

*CSnanoXRD investigation of the graded GBS-Si<sub>x</sub> coating annealed at 1100°C*

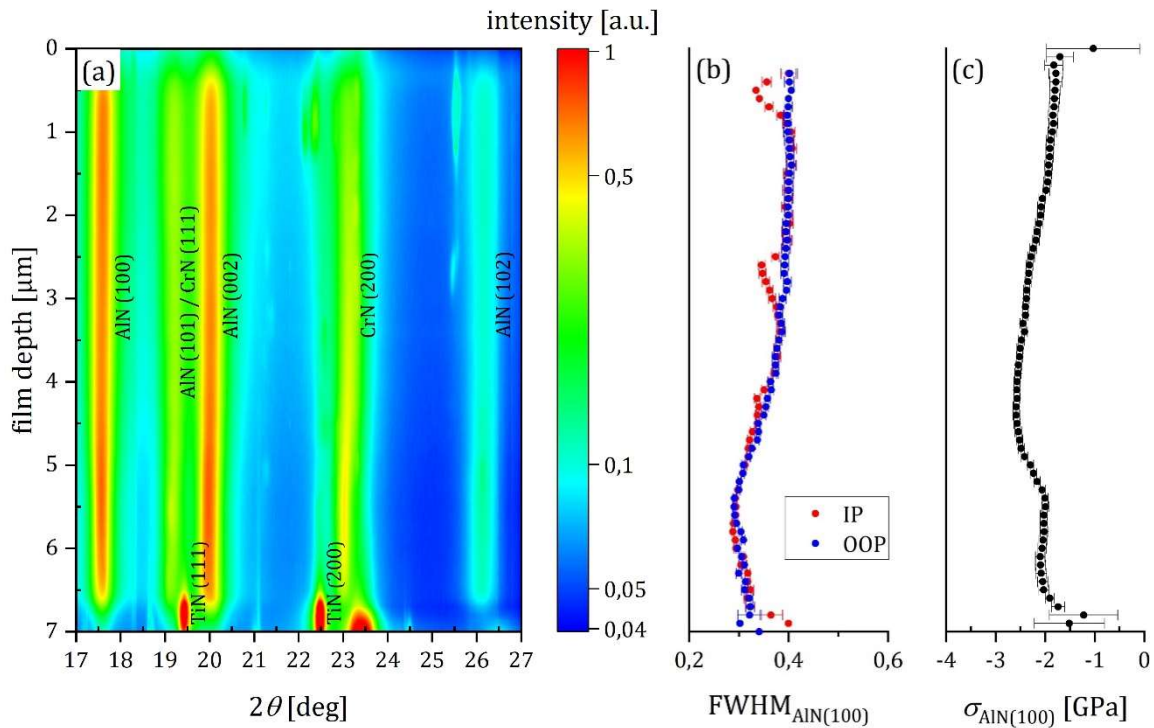


**Figure 16:** (a) Diffraction intensity distribution from the GBS-Si<sub>x</sub> coating heated at 1100°C shows maxima of the wurtzite AlN and cubic CrN phase as well as reflections from the TiN bonding layer at higher coating depth. Further analysis of the AlN (100) reflection reveals an influence of the heat treatment on the FWHM (b) and the stress (c).

Also after annealing up to 1100°C, the phase plot in Fig 16a suggests the perseverance of the w-Al(Cr)N and c-Cr(Al)N phases in the coating after the heat treatment up to 1050°C (Fig 16a). In addition, the positional shift of the CrN 200 reflection and the increase of the FWHM between 5.5 and 4.5 μm are still visible.

Similar to case of the GBS-Si<sub>x</sub> coating annealed at 1050°C, the FWHM also indicates a segregation-induced decrease of the size of coherently diffracting domains in the lower part of the coating. (Fig 16b).

The compressive stress starts at -1.51 GPa and reaches values of up to -2.58 GPa at the coating depth of 4.4 μm, from where a steady decline and therefore pronounced stress relaxation down to -1.7 GPa was determined.

## Cross-Sectional X-ray Nanodiffraction – SAXS

Generally, the SAXS signal is sensitive to changes in the electron density within the gauge volume. Therefore, periodic microstructures in the coatings show SAXS reflections, from which the nanolayer periodicity can be calculated. In this section, a focus is taken on the evaluation of the influence of Si on the properties of the nanolayers.

### *SAXS investigation of the graded GBS-Si<sub>x</sub> coating in as-deposited state*

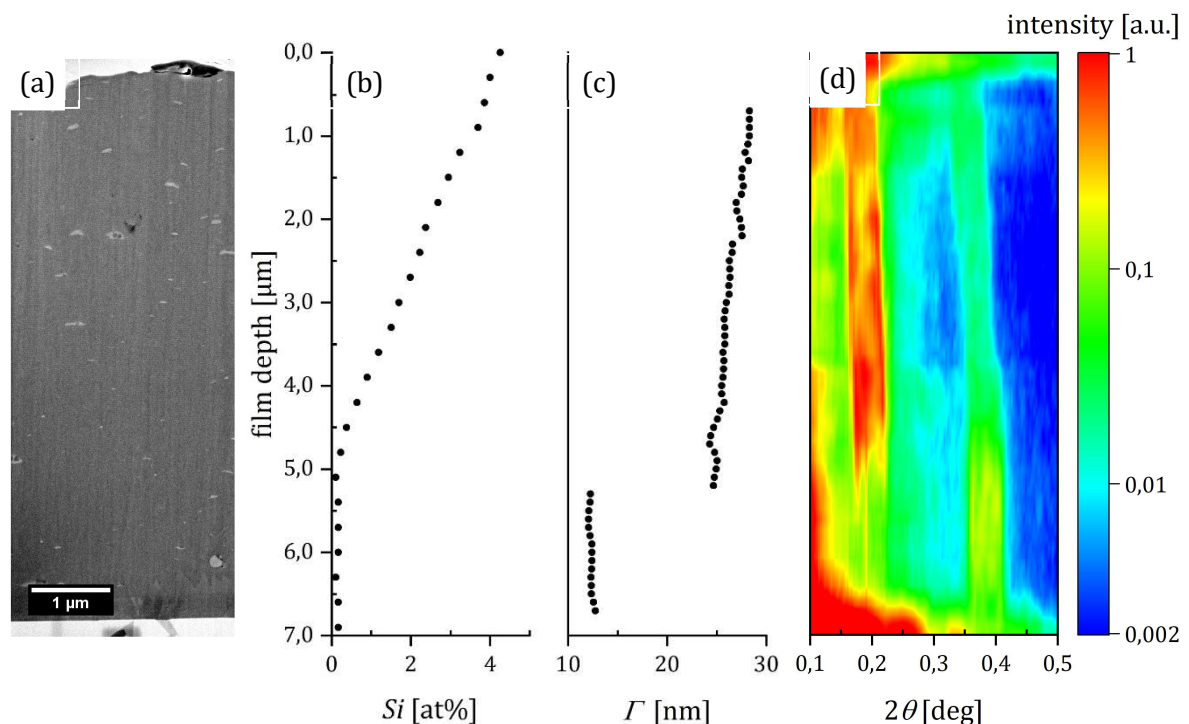


**Figure 17:** An SEM micrograph of the cross-section of the GBS-Si<sub>x</sub> coating (a) in addition to the measurement of Si content (b) reveals the formation of a nanolayered structure of a periodicity  $\Gamma$  (c) which can be extracted from the correlating SAXS diffractogram in (d).

At the early stages of the coating growth, at the coating depths between  $\sim 5.5$  and  $6.5$   $\mu\text{m}$ , the SAXS signal (Fig. 17d) can be related to the periodic changes of the Al/Cr ratio within the coating, which are caused by alternating evaporation of Cr and Al from the respective cathodes. Through every full rotation of the substrate carousel, the coating passes twice by a stack of the Al<sub>0.8</sub>Cr<sub>0.2</sub> cathodes leading to formation of the two layers per rotation (*cf.* Methods/Experimental). The nanolayer periodicity starts at 12 nm reflected by a 1<sup>st</sup> order SAXS reflection at  $2\theta = 0.4$  deg (Fig. 17c,d). A jump to 24 nm is detected at the 5  $\mu\text{m}$  coating depth, which corresponds to the initiation of SiH<sub>4</sub> from the gas inlet (Fig. 17b,c). The further period



increases up to 28 nm is attributed and correlated to the increasing amount of Si in the coating (Fig. 17b). As Si is introduced at only one point during the rotation of the substrate carousels, the periodicity of the nanolayers changes, which is reflected by a change of the 1<sup>st</sup> order SAXS signal at  $2\theta = 0.2 \text{ deg}$  corresponding to the nanolayer periodicity of 28 nm (Fig. 16c, d). With the increasing Si-content, the nanolayer periodicity increases, which can also be seen by a further decrease of the position of the SAXS 1<sup>st</sup> order reflection in Fig. 17c.

### *SAXS investigation of the graded GBS-Si<sub>x</sub> coating annealed at 1000°C*

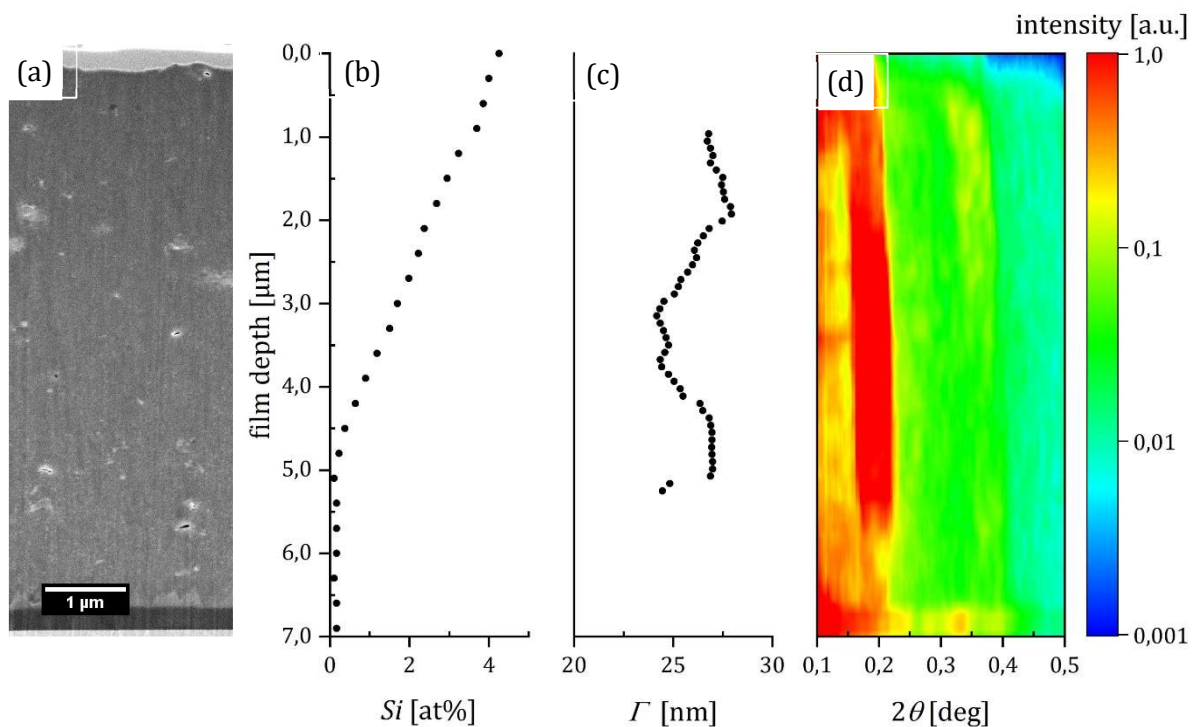


**Figure 18:** A SEM micrograph from the cross-section of the GBS-Si<sub>x</sub> coating annealed at 1000°C (a) in addition to the cross-sectional Si distribution (b) reveals the formation of a nanolayered structure with a periodicity  $\Gamma$  (c) which was extracted from the correlating SAXS diffractogram (d).

The SAXS intensity plot shows the 1<sup>st</sup> order SAXS reflection at  $2\theta = 0.2 \text{ deg}$  between 0 and 5  $\mu\text{m}$  coating depth, but no distinguishable reflection at  $2\theta = 0.4 \text{ deg}$  (Fig. 18d). Therefore, the periodic changes of the Al/Cr ratio within the coating have either been (i) randomized or (ii) equalized by the heat treatment, whereas periodic imbalances caused by the Si are still present and show a nanolayer periodicity of 26 nm (Fig. 18c). These findings are in agreement with the microstructure data presented in Fig 10.

*SAXS investigation of the graded GBS-Si<sub>x</sub> coating annealed at 1050°C*

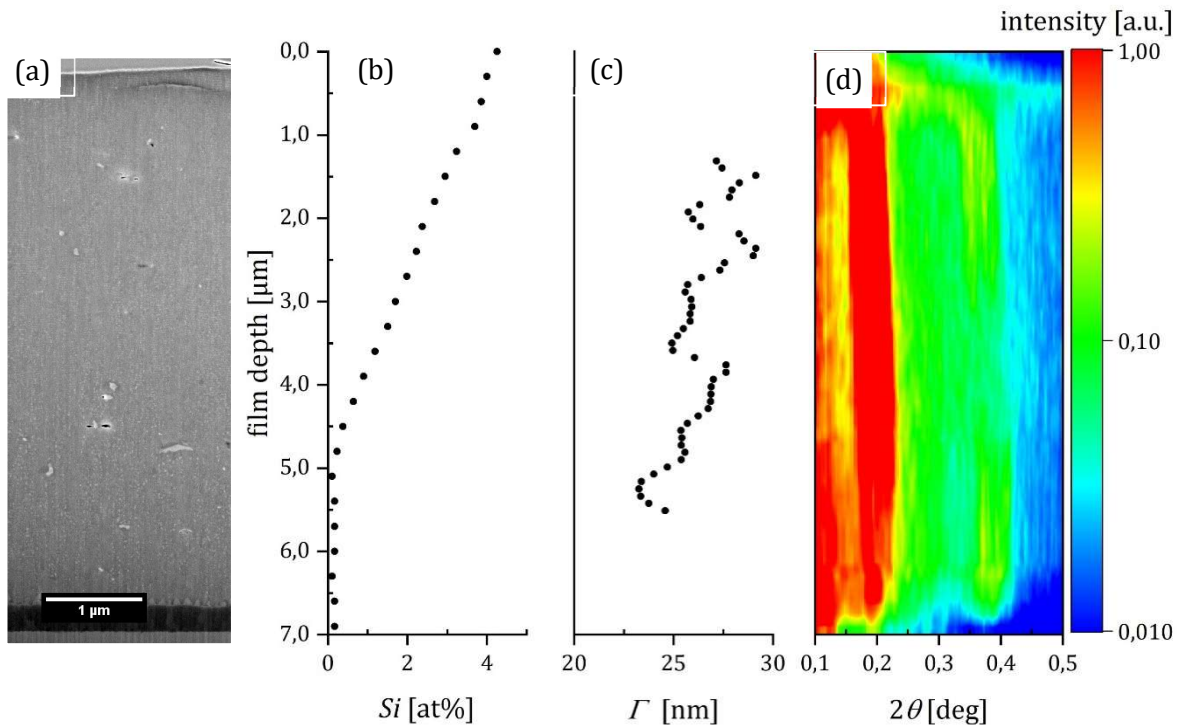


**Figure 19:** A SEM micrograph of the GBS-Si<sub>x</sub> coating cross section annealed at 1050°C (a) in addition to the measurement of Si content (b) reveals the formation of a nanolayered structure of a periodicity  $\Gamma$  (c) which was extracted from the cross-sectional SAXS data (d).

The SAXS intensity plot shows the 1<sup>st</sup> order SAXS reflection at  $2\theta = 0.2$  deg, from which an average nanolayer periodicity of 26nm can be calculated using Bragg's law (Eq. 1) (Fig. 19c,d).

As previously stated the missing reflection at  $2\theta = 0.4$  deg (Fig. 19d) indicates that the chemical imbalances in the Al/Cr ratio close to the substrate/coating interface have been equalized.



## SAXS investigation of the graded GBS-Si<sub>x</sub> coating annealed at 1100°C

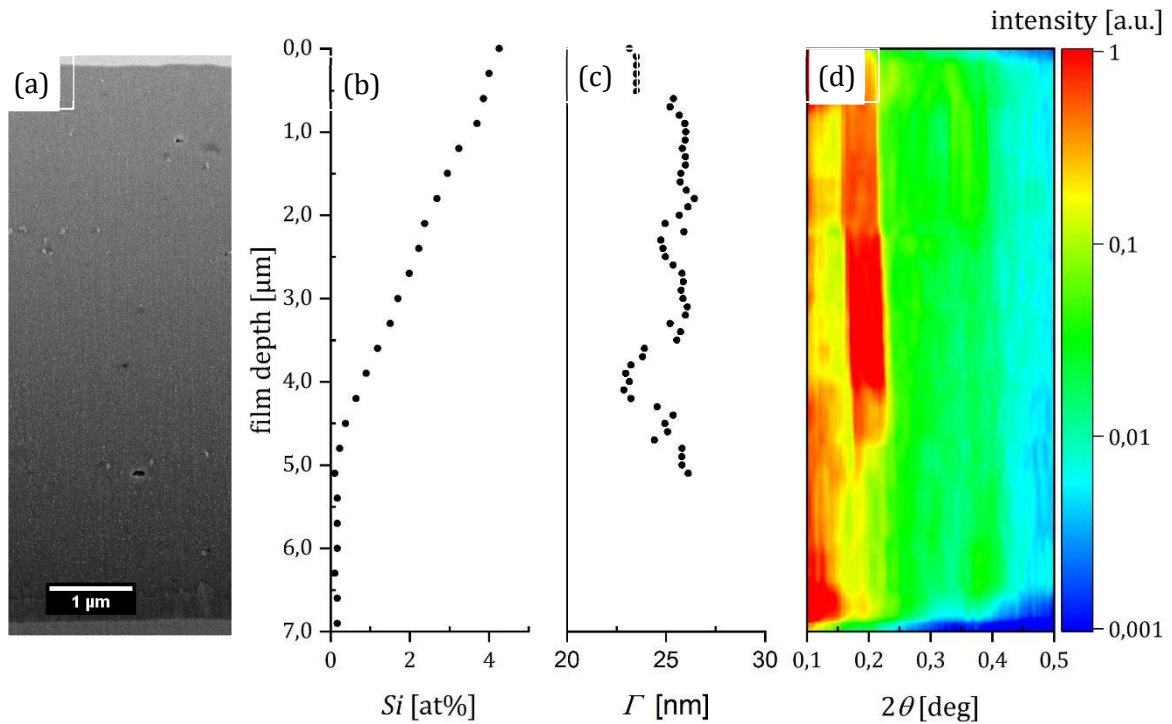


**Figure 20:** The GBS-Si<sub>x</sub>-1100°C cross section (a) in addition to the measurement of Si content (b) reveals the formation of a nanolayered structure of a periodicity  $\Gamma$  (c) which was evaluated from the cross-sectional SAXS data (d).

The SAXS intensity plot shows the 1<sup>st</sup> order SAXS reflection at  $2\theta = 0.2 \text{ deg}$  only from the surface to  $\sim 4.5 \mu\text{m}$ , from which position an average nanolayer periodicity of  $\sim 25 \text{ nm}$  was evaluated. This indicates, that the coating exhibiting low Si contents is already affected by the heat treatment and justifies that an annealing temperature of 1100°C is too high for a separation of segregating and non-segregating sublayer, which was the premise for this thesis.

## Cross Sectional Nanoindentation

In this section the mechanical properties of the gradient coating were evaluated in order to further select (i) the chemical composition of the alternating sublayers within the multi-layered coatings (Table 1) and (ii) the appropriate heat treatment.

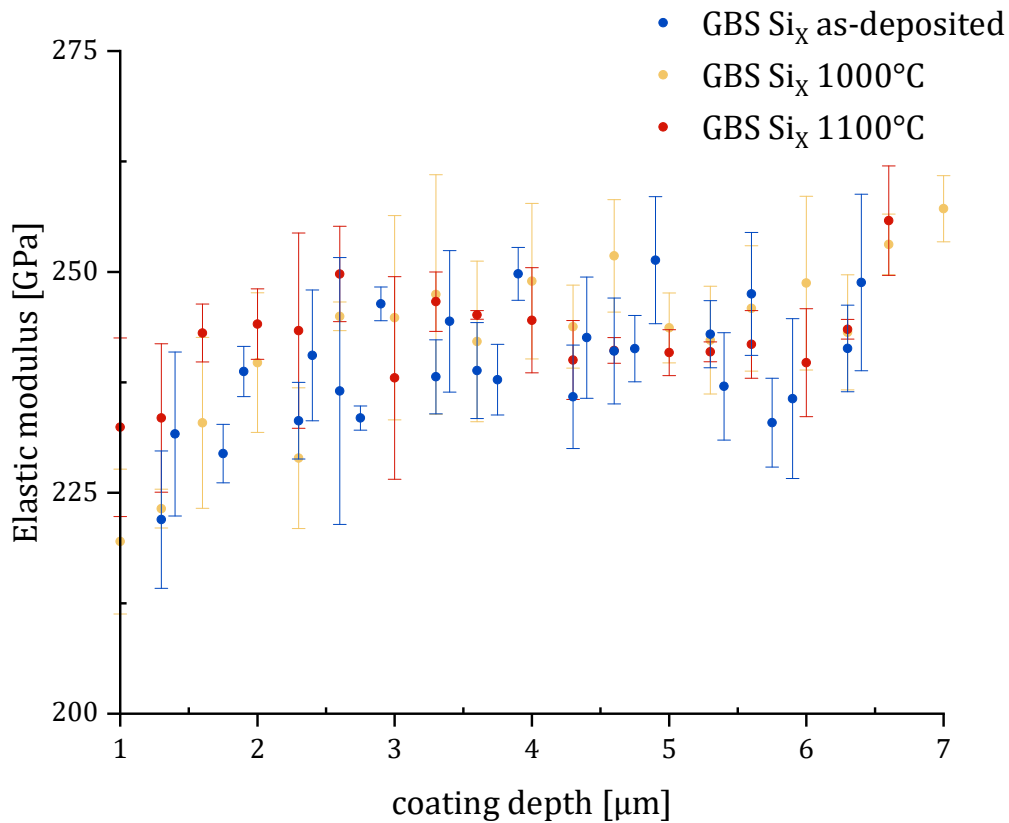


**Figure 21:** The indentation modulus was measured as a function of the coating depth by nanoindentation for the GBS-Si<sub>x</sub> gradient coating in as-deposited state as well as after annealing.

In Fig. 21, the depth distributions of the indentation moduli obtained by the nanoindentation for the coating depths of 1-7 μm are presented. Smaller coating depths were excluded as an influence of the coating surface on the indentation couldn't be excluded.

The indentation moduli of the as-deposited coating ranges from 221 - 248 GPa (Fig. 21 GBS-Si<sub>x</sub>-ad), which is in agreement with the findings from *in situ* cantilever bending experiments for the as-deposited GBS-Si<sub>0</sub> and GBS Si<sub>10</sub> samples (Fig. 27). For the same coating after the annealing up to 1100°C, a range of 232 - 255 GPa (Fig. 21 GBS-Si<sub>x</sub>-1100°C) was measured, which is in contrast to the findings from the respective *in situ* cantilever bending experiments on the GBS-Si<sub>0</sub> and GBS Si<sub>10</sub> samples in their annealed state (Fig. 27).

Especially at the coating depths from 5 – 7  $\mu\text{m}$ , which marks the Si free part of the coating the elastic modulus remained rather unaffected by the thermal exposure in contrast to the later present findings from *in situ* cantilever bending experiments. However, at the coating depths below 3  $\mu\text{m}$  where the Si content is greater than 2% (Fig. 8) a higher modulus after the annealing at 1000° is observed.

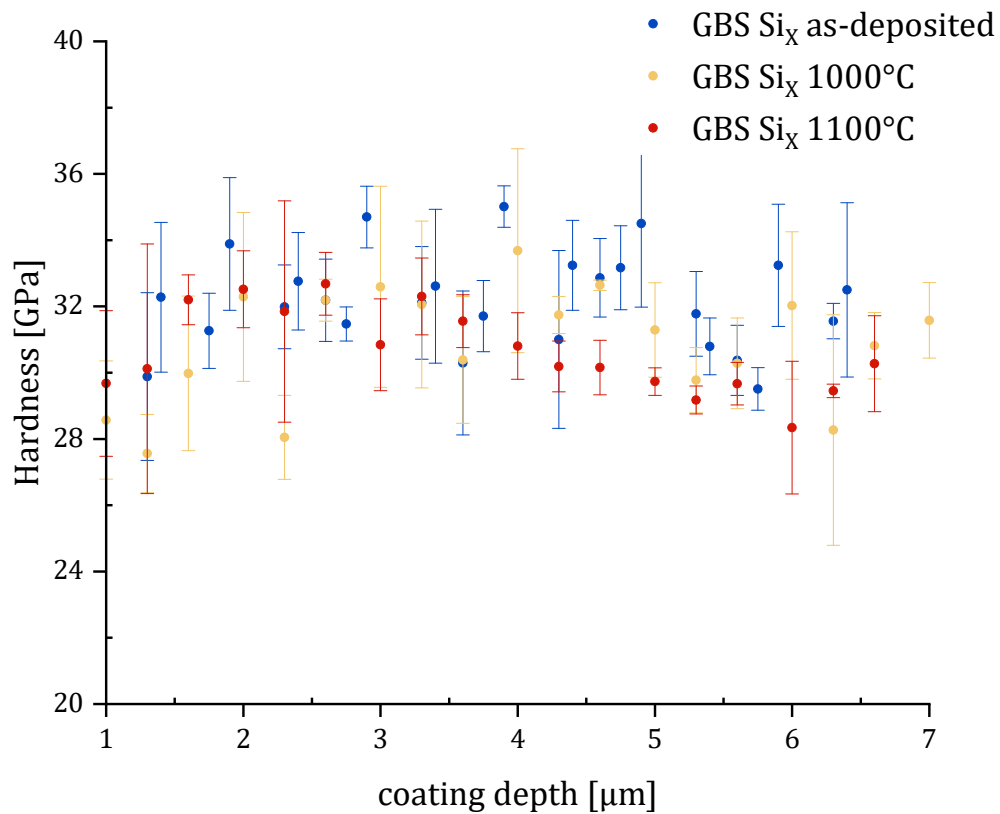


**Figure 22:** A depth distribution of the hardness across the graded GBS  $\text{Si}_x$  coatings determined by nanoindentation.

In Fig. 22 the hardness results evaluated from nanoindentation experiments for coating depths from 1 - 7  $\mu\text{m}$  are listed. They range from 29 to 35 GPa for the as-deposited coating, as well as 28-34 GPa after annealing at 1000°C and at last between 28 and 33 GPa.

A decrease in hardness can be observed for GBS- $\text{Si}_x$ -1100°C coating compared to the GBS- $\text{Si}_x$ -ad at the coating depths higher than 5  $\mu\text{m}$  (Fig. 22). At lower coating depths the hardness of these two coating are within the same range. This can be seen as an indication that the addition of Si stabilizes the hardness during the thermal exposure.

# Microstructural analysis and *ex situ* fractography

In this section the fracture modes before and after heat treatment are compared. Further the question is answered if a multilayered coating has an influence on the crack propagation.

## *Microstructure and fracture surface analysis of the reference GBS-Si<sub>0</sub> coating*

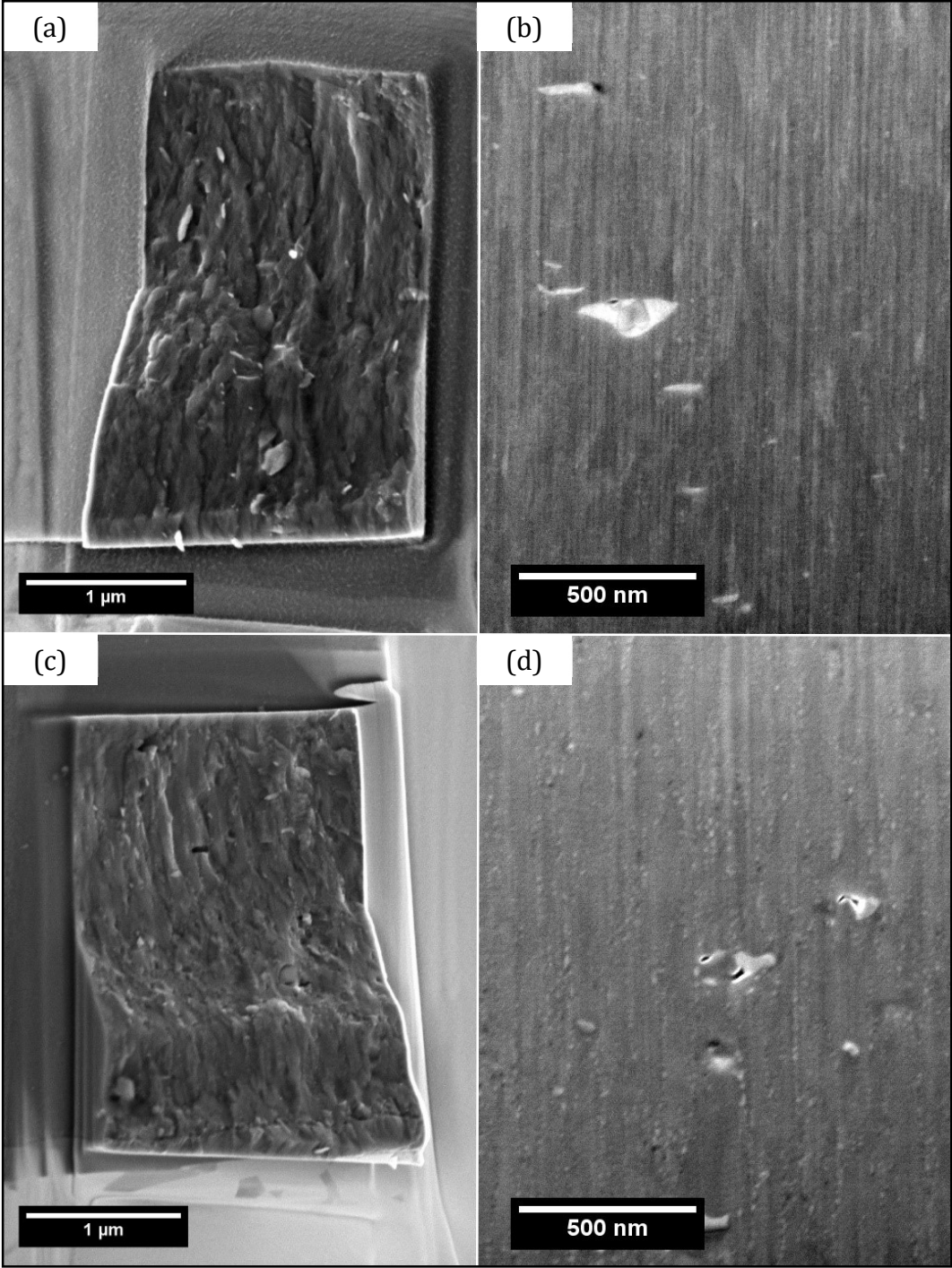


**Figure 23:** SEM images of a GBS-Si<sub>0</sub>-ad coating fracture surface (a) with an image of the FIB cross section (b) compared to the fracture surface after the heat treatment (c) and corresponding microstructure (d).

From a structural viewpoint, columnar grain can be observed both in Figs. 23b and d, which depicts the GBS-Si<sub>0</sub> coatings in as-deposited and heat-treated state, respectively. At the first sight, the microstructure is only interrupted by droplets and pores. Qualitatively, the grain size remained unaffected by the heat treatment (compare Figs. 23b and d), however in Fig. 23d a seam of precipitation has developed around the elongated grains. This is in close agreement with the microstructure found in the bottom part of the gradient coating (*cf.* Figs. 9 and 11c) and is caused by the precipitation of CrN.

Fractography on the cantilevers analysed in as-deposited state (Fig. 23a) shows clear vertical steps on the fracture surfaces, which are the free faces of elongated grains and therefore indicate intercrystalline crack propagation. The cantilevers fracture surface of the coating in heat-treated state (Fig. 23c) on the other hand show a smooth fracture surface with sparse facets of grains suggesting a mixed fracture behaviour with a significant amount of transcrystalline crack growth.

The pronounced curvature in both of these cleavage planes stems from the stress distribution within the cantilever. The crack avoids high compressive stresses at the lower restraint of the cantilever and therefore moves to shorter bending lengths (Figs. 23a,c). This feature is much more prominent for transcrystalline crack propagation.

*Microstructure and fracture surface analysis of the Si-alloyed  $(Al_{0,7}Cr_{0,3})_{0,9}Si_{0,1}N$  coating*

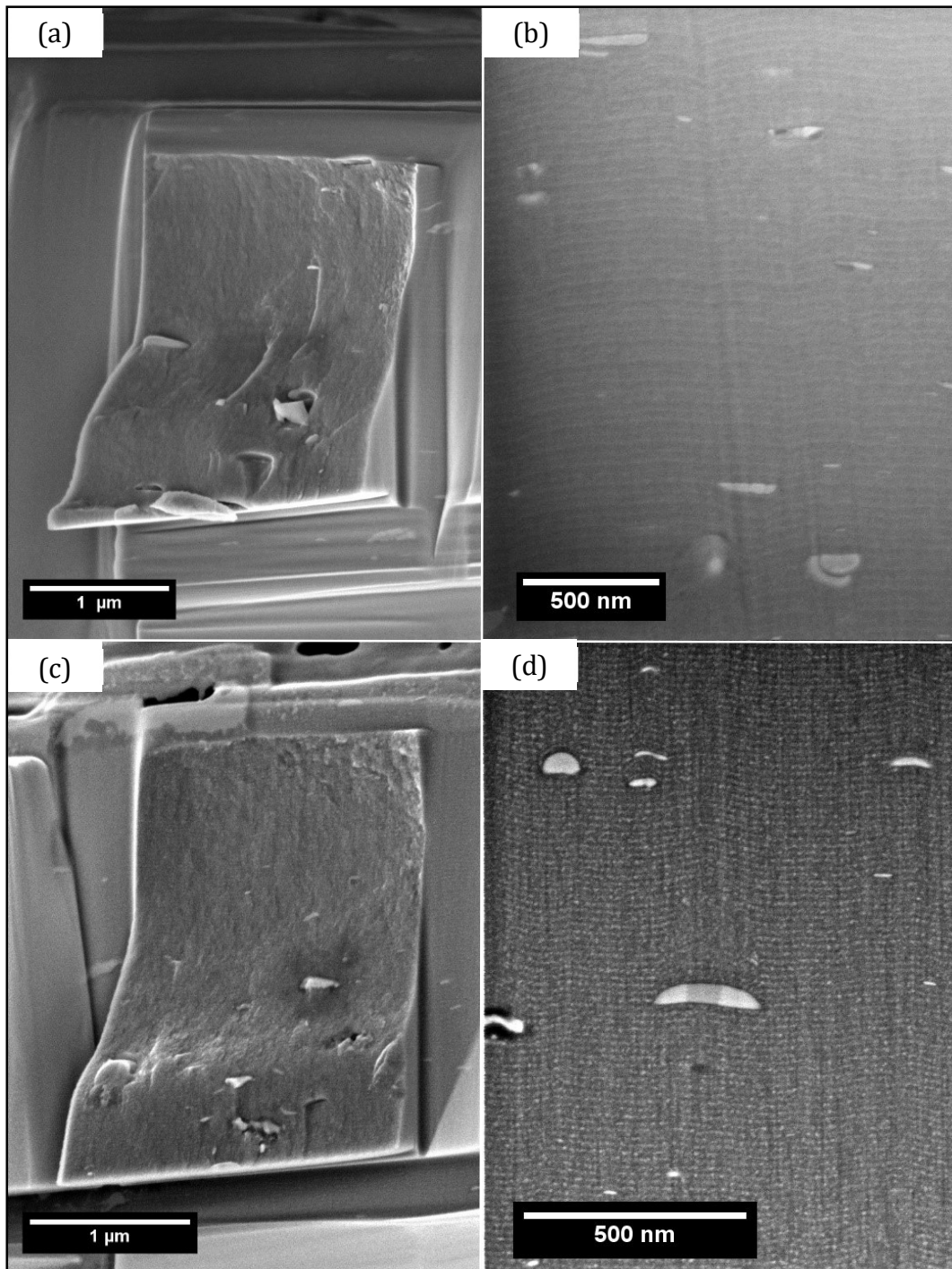


*Figure 24: A SEM image of a GBS-Si<sub>10</sub>-ad coating fracture surface (a) with an image of the FIB cross section (b) compared to the fracture surface after the heat treatment (c) and corresponding microstructure (d).*

As expected from the investigation of the gradient coating, the introduction of Si comes with the formation of a nanolayered microstructure (Fig. 24b), which coarsens after the annealing up to 1050°C, but remains ultimately intact (Fig. 24d). This correlates to the observed microstructure in Fig. 11b. Furthermore, it proves, that both compositions with and without Si are suitable candidates for the multilayer architecture, where the Si-free coating (Fig. 23) and the Si-containing coating (Fig. 24) promote trans-crystalline and inter-crystalline fracture upon loading, respectively.

Both fracture surfaces show a glassy morphology (Fig. 24a,c), characteristic for nanocrystalline materials. The annealed sample shows a coarsening compared to the as-deposited sample similar to the microstructure (Fig. 24b,d).

*Microstructure and fracture surface analysis of the multilayer structure with 500 nm thick  $Al_{0.8}Cr_{0.2}N$  sublayers (GBS-MI<sub>1</sub>)*

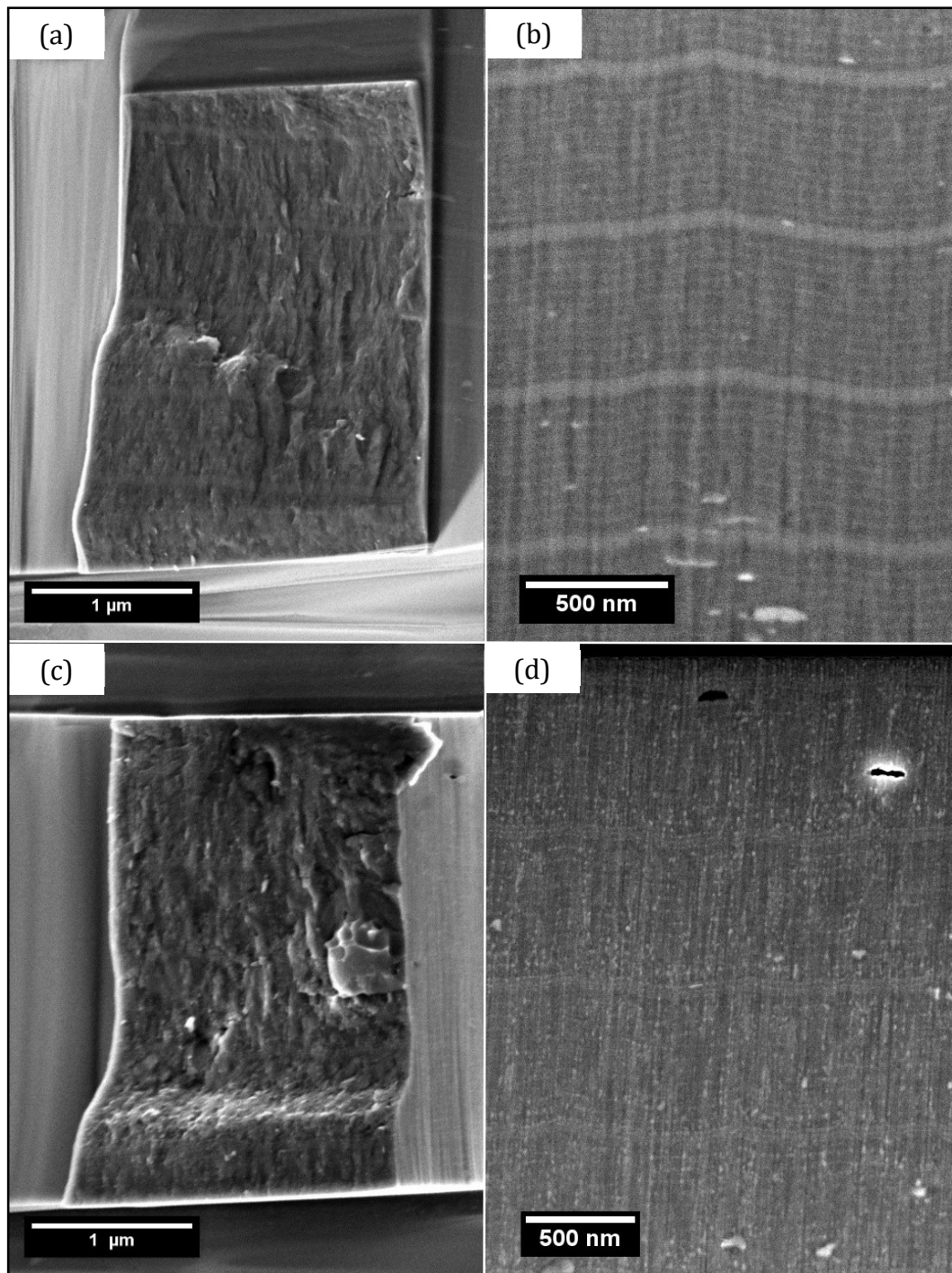


*Figure 25: A SEM image of a GBS-MI<sub>1</sub>-ad coating fracture surface (a) with an image of the FIB cross section (b) compared to the fracture surface after the heat treatment (c) and the corresponding microstructure (d).*



In Fig. 25b, the proposed microstructure of the multilayer coating is presented. Si-free  $\text{Al}_{0,8}\text{Cr}_{0,2}\text{N}$  sublayers of 500 nm in thickness are interrupted by 50 nm sublayers of  $(\text{Al}_{0,7}\text{Cr}_{0,3})_{0,9}\text{Si}_{0,1}\text{N}$  visible as thin interlayer's of higher brightness. The Si-free thick sublayers further show the nano-layered microstructure, which was also identified in the gradient coating in Fig. 9b and by SAXS (*cf.* Fig. 17).

After the annealing at 1050°C, the Si free thick sublayers show pronounced precipitations of CrN, whereas within the thin Si enhanced layers no such precipitations are visible. This verifies the concept of the multilayer coatings approach suggested within this thesis (Fig. 25d).

The fracture surface of the as-deposited sample shows elongated faces of elongated grains in the direction of the face propagation indicating inter-crystalline crack growth (Fig. 25a). The fracture surface of the annealed sample shows a distinct pore close to the surface which was the origin of fracture. The large steps radiating from it turn into a smooth surface at the lower edge of the cantilever indicating mixed fracture modes (Fig. 25c). Crack deflection caused by the interfaces of individual sublayers is however not visible.

*Microstructure and fracture surface analysis of the first multilayer structure with 250 nm thick  $Al_{0.8}Cr_{0.2}N$  sublayers (GBS- $Ml_2$ )*

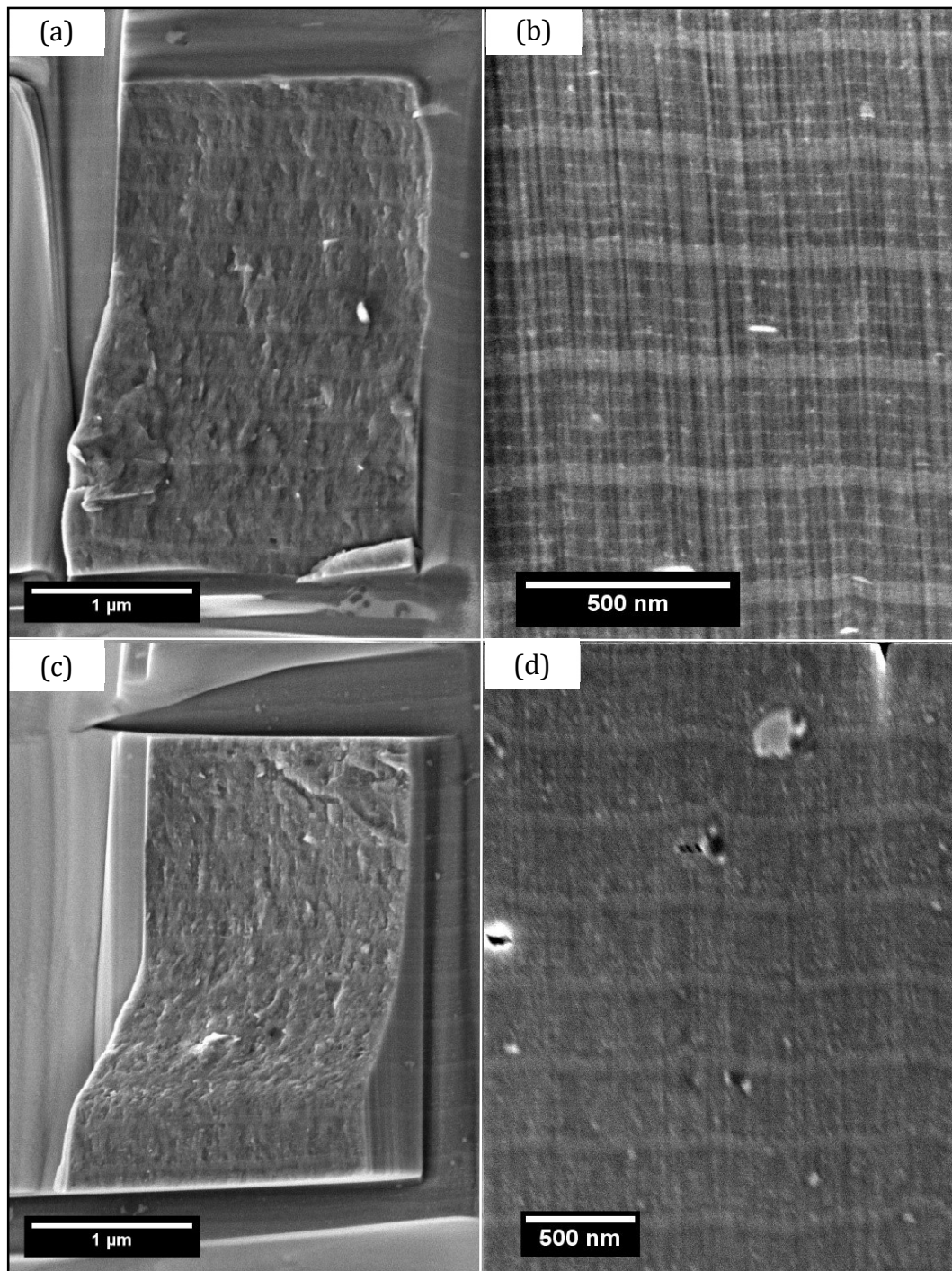


*Figure 26: A SEM image of a GBS- $Ml_2$ -ad coating fracture surface (a) with an image of the FIB cross section (b) compared to the fracture surface after the heat treatment (c) and the corresponding microstructure (d).*

In Fig. 26b the multilayered microstructure shows the same features as the coating presented in Fig. 25b, with thick sublayers of Si-free  $\text{Al}_{0,8}\text{Cr}_{0,2}\text{N}$  interrupted by thin sublayers of  $(\text{Al}_{0,7}\text{Cr}_{0,3})_{0,9}\text{Si}_{0,1}\text{N}$ . In order to investigate the influence of the interlayer thickness, here the layer thickness of AlCrN was reduced by half and is therefore only 250 nm. This results in a smaller number of nanolayers, as fewer rotations are made with the carousel in the deposition chamber, but also in a higher number of Si-enhanced and Si-free interlayers per cantilever.

The annealed microstructure in Fig. 26d is comparable with that in Fig. 27d of the previous multilayered coating, as larger grains of presumably CrN are visible within the Si-free parts of the coating but not in between.

The fracture surfaces of the respective cantilevers in Fig. 25a,c and Fig. 26a,c provide no evidence of crack deflection at the interfaces of the individual sublayers, also after the increase in the numbers of the passed interfaces. However, the rough fracture surface of the as-deposited cantilever in Fig. 26a, is in contrast to the smoother surface of the annealed cantilever, which also exhibits a dedicated curvature at the bottom part in Fig. 26c. Thereby, a change from inter-crystalline to trans-crystalline fracture by thermal exposure is indicated, as also found for the Si-free coating (Fig. ???).

## Mechanical properties obtained by *in situ* cantilever bending

In this section, the mechanical properties determined from in-situ micromechanical experiments on FIB-prepared cantilever are outlined at first in Table 2 and then reformatted additionally in Figs. 27-29 for further comparison of the different sample systems. The elastic modulus and fracture stress were measured by loading of unnotched cantilevers until fracture, whereas the fracture toughness was retrieved by fracturing intentionally pre-notched cantilevers (cf. Methods, *In situ* Cantilever bending).

**Table 2:** An overview of the mechanical properties of the two multilayer coatings GBS- $ML_1$  and GBS- $ML_2$ , as well as the reference coatings GBS- $Si_0$  and GBS- $Si_{10}$ .

Sample Name	Elastic Modulus [GPa]	Fracture Stress [GPa]	Fracture Toughness [MPa m <sup>1/2</sup> ]
GBS- $Si_0$ -ad	208 ± 16	3.4 ± 0.3	2.5 ± 0.1
GBS- $Si_0$ -ht	289 ± 7	4.3 ± 0.5	2.5 ± 0.1
GBS- $Si_{10}$ -ad	250 ± 24	4.6 ± 0.6	2.4 ± 0.3
GBS- $Si_{10}$ -ht	251 ± 11	4.0 ± 0.5	2.8 ± 0.3
GBS- $ML_1$ -ad	239 ± 6	3.8 ± 0.4	2.7 ± 0.3
GBS- $ML_1$ -ht	231 ± 28	4.7 ± 0.5	2.6 ± 0.1
GBS- $ML_2$ -ad	248 ± 6	3.2 ± 0.3	2.3 ± 0.2
GBS- $ML_2$ -ht	221 ± 11	4.0 ± 0.5	2.4 ± 0.1

The mechanical properties presented in Table 2 are mean values obtained from micromechanical experiments on at least 3 different cantilevers.

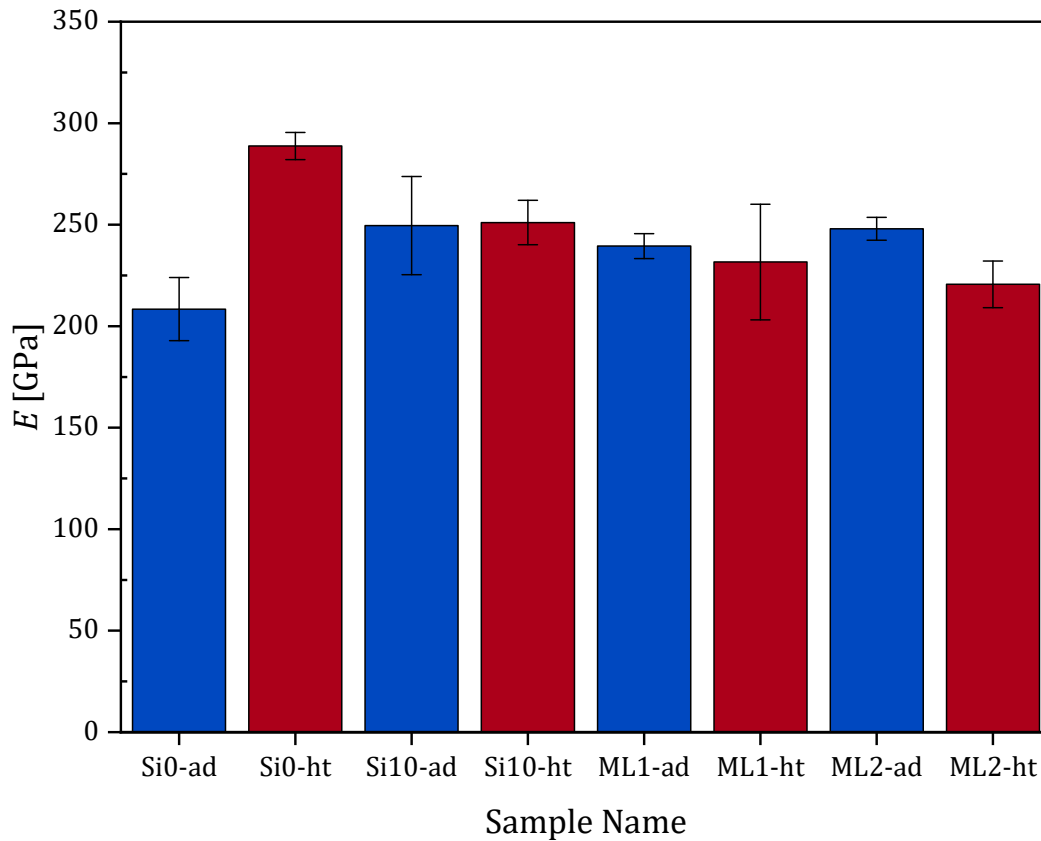


*Figure 27: Comparison of the elastic moduli of different coating sample systems obtained from micromechanical tests.*

In Fig. 27, the values of Young's moduli obtained from the unnotched micro-cantilever beam specimens are displayed. It can be seen, that the Si-free reference GBS-Si<sub>0</sub> coating has a Young's modulus of 208 GPa in as-deposited state, while the addition of 10% Si to the AlCrN coating raises its elastic modulus in as-deposited state to 250 GPa. Comparatively, in the annealed state the Si-free coating shows a pronounced increase of stiffness up to 289 GPa, whereas Si<sub>10</sub>-ht remained with 251 GPa similar to its as-deposited counterpart. For the GBS-Si<sub>0</sub> coating it can be seen that due to grain boundary segregation the modulus rises by ~80 GPa or ~40% compared to the as-deposited state. Contrary, the elastic properties of the Si-containing coating remain unaffected by the heat-treatment, as intentionally planned for this coating.

From the elastic data, the elastic moduli evaluated from the two multilayer coatings GBS-ML<sub>1</sub> and GBS-ML<sub>2</sub> are within 220 – 248 GPa and are also not significantly affected by the thermal treatment.

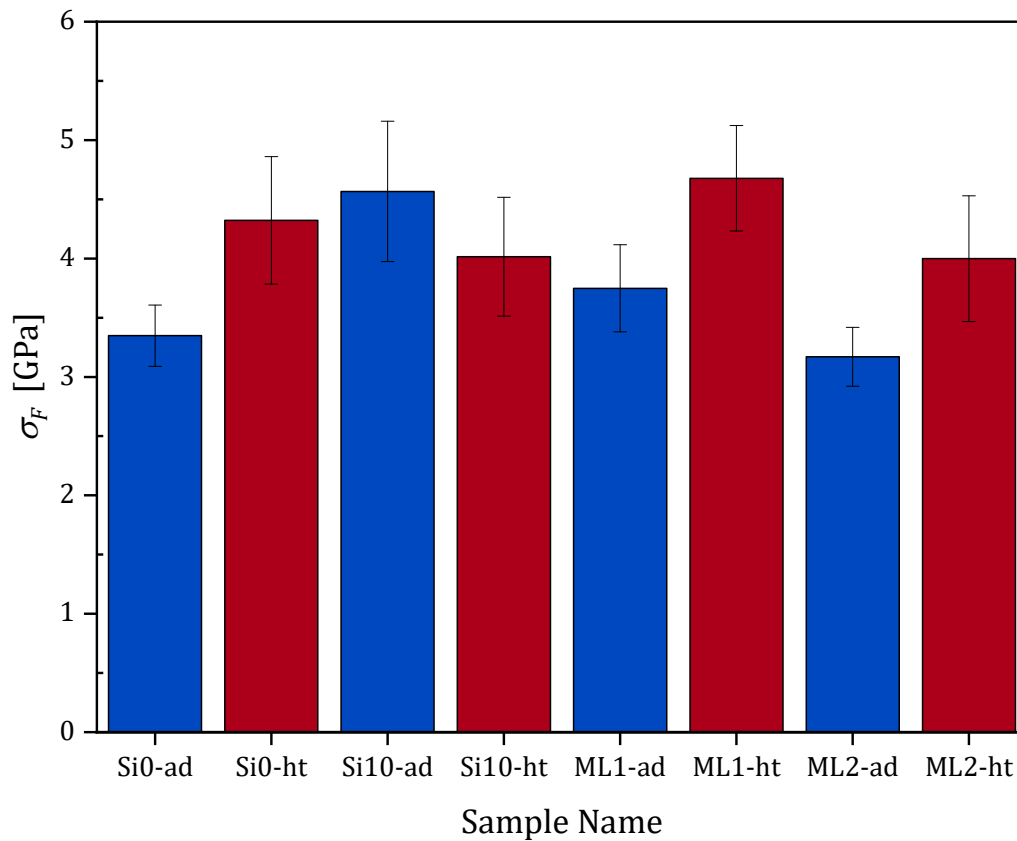


**Figure 28:** Comparison of fracture stresses of different coating sample systems obtained from micromechanical tests.

Much alike to the elastic moduli, the fracture stress increases from 3.4 to 4.3 GPa after applying the heat treatment on the Si-free GBS-Si<sub>0</sub> coating. It shows, that the grain boundary segregation induced by the heat treatment is very effective to tailor the fracture stress. Contrary, when Si-containing coating is subjected to the heat treatment the fracture stress is reduced from 4.6 to ~4 GPa. However, this decrease is within the intersection of the standard deviations of the as-deposited and annealed state and therefore not conclusive.

But, whereas the elastic modulus of the multilayer coatings remained indifferent to the thermal exposure, a distinct increase in fracture stress could be observed for both samples from 3.8 to 4.7 GPa (Fig. 28, ML<sub>1</sub>) and from 3.2 to 4.0 GPa (Fig. 28, ML<sub>2</sub>), respectively. This improvement is in the same range of the Si-free Al<sub>0.8</sub>Cr<sub>0.2</sub>N coating (Fig. 28 Si<sub>0</sub>), in detail ~0.8 GPa.

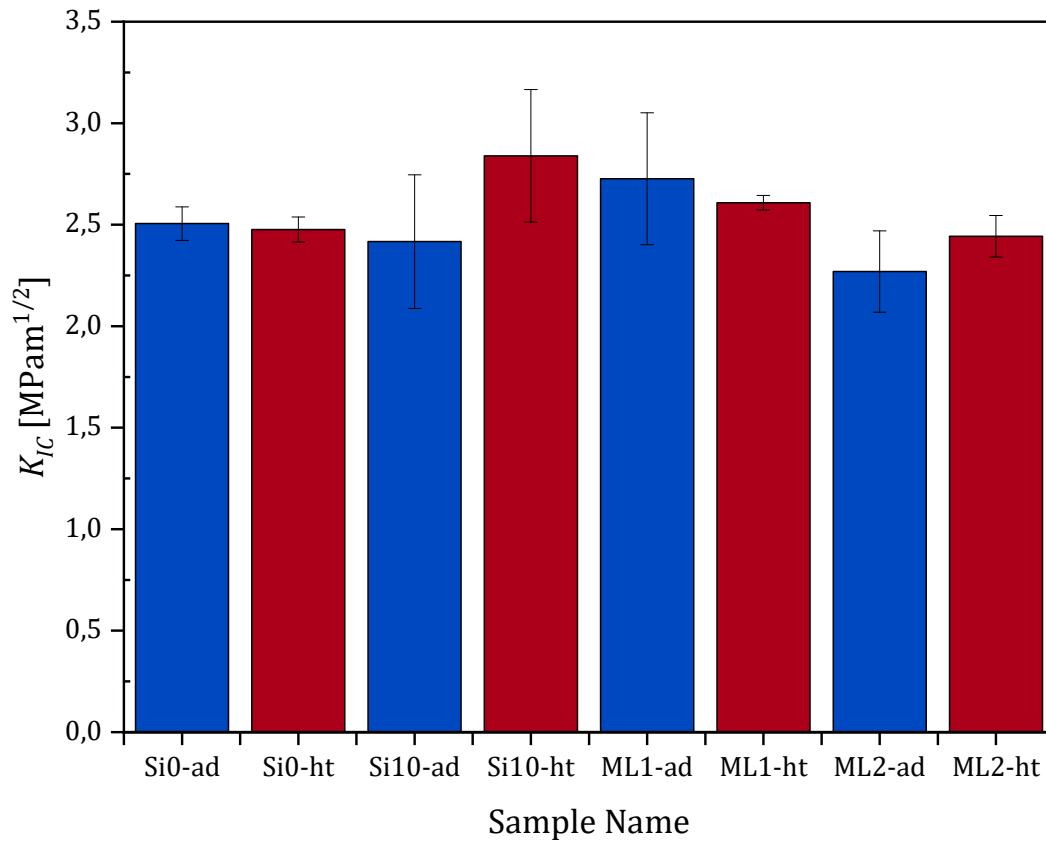


**Figure 29:** Comparison of the fracture toughness of different coating sample systems obtained from micromechanical tests.

An overall variation of fracture toughness values between 2.3 to 2.8 MPam<sup>1/2</sup> was measured for the tested AlCrN coatings and is provided in Fig. 29. With the exception of the (Al<sub>0,7</sub>Cr<sub>0,3</sub>)<sub>0,9</sub>Si<sub>0,1</sub>N coating (GBS-Si<sub>10</sub>), the fracture toughness of each annealed coating stayed within ±0.1 MPam<sup>1/2</sup> of their as-deposited counterpart. GBS-Si<sub>10</sub> displayed a fracture toughness of 2.4 MPam<sup>1/2</sup> in its as-deposited and 2.8 MPam<sup>1/2</sup> in its annealed state.

Therefore, changes, which observed in the microstructure (*cf.* Fig. 25 and Fig. 26) and fracture stress (Fig. 28) could not be transferred to the fracture toughness of the respective cantilevers.

### *Microstructural evolution of the coatings upon annealing*

Observations on the composition and the microstructure of the gradient coating GBS-Si<sub>x</sub> revealed periodic changes of the Al/Cr ratio across the coating depth (Figs. 8,9), caused by the deposition process. The carousel passes a stack of Al<sub>0.8</sub>Cr<sub>0.2</sub> cathodes twice during one rotation in the deposition chamber, which results in the formation of a periodic nanoscale variation of the Al to Cr ratio (Fig. 9), which could be also confirmed by the SAXS-reflection at 0.4 deg (Fig. 17). Its disappearance after the annealing of up to 1000°C (Fig. 18) could be related to the segregation of Cr to clusters and the ongoing formation of CrN countering the periodic changes in the Al to Cr ratio. This is affirmed by the increased intensity of the 200 CrN reflection after the annealing (Fig. 14).

A change in the position of the 1<sup>st</sup> order SAXS reflection was observed shortly after the addition of SiH<sub>4</sub> to the process gas (Fig. 17). The nanolayer periodicity doubled, which is reasonable as SiH<sub>4</sub> is only introduced at one point during the rotation of the carousel. Similar observations could be observed for TiAlON coatings, where O was also introduced via a gas lance leading to a periodic variation of the O content within the coating in Ref. [40]. Within their work, TEM investigation revealed that the periodic change in the chemical composition didn't influence the microstructure of grains crossing multiple nanolayers. Therefore, the conclusion can be drawn that these nanolayers don't enhance mechanical properties of hard coatings.

### *Development and relaxation of residual stresses in nanolayered coatings*

The development of compressive residual stresses during film growth can be attributed to three different origins. First of all, extrinsic stress components stem from structural misfits, phase transformations and precipitations. Complementary intrinsic stress components are build up by atomistic processes during film growth and the generation of volume increasing defects. These two contributions are completed by the thermal stress component which is caused by different thermal expansion coefficients of the prominent phases [41].



The compressive stress in our gradient coating stabilized at first in the range of -1.7 GPa (Fig.13) in the Si-free part of the coating. With the introduction of Si, the compressive stress starts to rise again and reaches values of up to -2.69 GPa. This can be attributed to a higher defect density in the nanocomposite structure, further indicated by the greater FWHM and the difficulties of the Al<sub>80</sub>Cr<sub>20</sub>N matrix to incorporate Si. Jäger *et al.* [21] found stresses of up to -4.9 GPa in w-Al<sub>90</sub>Cr<sub>10</sub>N coatings deposited by similar process parameters. This can be explained by the formation at hexagonal phase. They further measured stresses of up to -3GPa in a multilayered c-Al<sub>70</sub>Cr<sub>30</sub>N/w-Al<sub>80</sub>Cr<sub>20</sub>N coating, which microstructure is more comparable to the nanolayered structure in our coatings.

Overall it can be seen that at 1050°C (Fig. 15), the relaxation of the growth induced stresses within the coating starts as the compressive stress decreases from -3.5 GPa at 2.5µm coating depth down to -3 GPa at the surface. This effect is even stronger pronounced after annealing up to 1100°C (Fig. 16). The difference in the 1050°C sample in total stress level can be correlated to the different substrate used for the deposition. After the comparison of the thermal expansion coefficient for steel, which can be estimated as  $11 \times 10^{-6} \text{ K}^{-1}$  [42] to the thermal expansion coefficients of cemented carbide between  $5\text{-}6 \times 10^{-6} \text{ K}^{-1}$  [43], the assumption can be made that the significantly higher expansion of steel during annealing causes the higher stress level afterwards.

### ***Improvement of Mechanical properties by Grain Boundary Segregation Engineering***

Due to the fact that micromechanical cantilever bending experiments are quite rarely performed, especially on w-AlCrN, stiffness and fracture stress can only be compared to indentation modulus and hardness data available in literature. In the case of pure c-AlCrN, elastic moduli of up to 430 GPa were reported in the as-deposited state, which could not be stabilized and decreased significantly after the annealing [8, 20, 42]. Contrary the w-Al(Cr)N coating in this thesis displays a lower elastic modulus of 208 GPa in as-deposited state, which however increases after annealing up to 289 GPa (*cf.* Table 2). This is related to the formation of c-CrN precipitates at the grain boundary probably blocking the weak underdense columnar grain boundaries. (*cf.* Fig. 9 – Fig. 12), thus forming a composite coating.

The investigation of c-AlCrN further showed that the addition of Si at 5% resulted in an overall decrease of the modulus down to 333 GPa compared to c-AlCrN in the as-deposited state. After the annealing at 1100°C for 30 min, the elastic moduli increased by ~10% to 360 GPa [20]. The drop in modulus for the as-deposited state with the increasing Si content is attributed to its tendency to destabilize the cubic metastable solid solution and thus to promote the formation of the softer hexagonal phase. The Si-alloyed w-Al(Cr)N coating tested in this thesis displays no change in elastic modulus or fracture stress during heating to 1050°C for 5 min (*cf.* Table 2, Fig. 27, Fig. 28). This can be attributed to the increased thermal stability of the phases and the microstructure by the addition of Si into the coating, as indicated also by WAXD and SAXD CSnanoXRD analysis (*cf.* Fig.13-20).

The analysis of the fracture stress (Fig. 28) shows a significant increase via Si-addition in as-deposited state compared to w-Al(Cr)N. This can be attributed to the formation of a nanocomposite coatings with amorphous hard  $\text{Si}_x\text{N}_y$ , which surrounds the encapsulated w-Al(Cr)N grains. This is supported by the glass-like fracture morphology shown in Fig. 24 and also reported in [20]. No changes of the fracture morphology occur even after annealing at 1050°C for 5 min and the fracture stress remained constant. Contrary, significant hardening supported by the pronounced increase of fracture stress was found for all w-Al<sub>0.8</sub>Cr<sub>0.2</sub>N containing coatings (*cf.* Table 2, Fig. 28), which could be reflected by an increase of hardness using indentation experiments. Reiter et al. [8] found an increase in hardness for w-Al<sub>0.83</sub>Cr<sub>0.17</sub>N coatings when annealing at temperatures up to 1300°C for 2h was applied, in contrast to Sabitzer *et al.* [44], where a decrease of hardness was reported for w-Al(Cr)N upon annealing for 1h. Both studies confirm that the annealing time is crucial for triggering the right amount of segregation. In general, all the heat treated w-Al<sub>0.8</sub>Cr<sub>0.2</sub>N displayed rather smooth fracture surfaces, attributed to a transcrystalline fracture mode, which affirms the chosen annealing parameters and the concept proposed within this thesis.

High temperature fracture toughness measurements for c-AlCrN coatings and AlCrSiN coatings were performed by Drnovšek *et al.* [45], where it was shown that upon annealing to only 600°C fracture toughness of c-AlCrN deteriorate with a final value of 1.1 MPam<sup>1/2</sup>, while AlCrSiN provided more resistance to the heat treatment and remained at 1.7 MPam<sup>1/2</sup>. Mechanical characterization after annealing is more prominent for TiAlN coatings, which can be related to the pronounced spinodal decomposition leading to hardening-by-annealing [46].

In the work of Bartosik *et al.* [47], self-toughening mechanism for  $Ti_{1-x}Al_xN$ , by nano-twinning and formation of distorted hexagonal AlN led to an increase of fracture toughness from 2.7 to 3.0  $MPam^{1/2}$  after the annealing to 900°C. Interestingly, annealing at 1000°C resulted in a fracture toughness of 2.8  $MPam^{1/2}$ , with no prominent toughening.

Unfortunately, no similar effects could be observed for the coatings with the dedicated grain boundary segregation, where no toughening upon annealing could be observed, despite the beneficial fracture stress and Young's modulus data. In this thesis, significant toughening could be observed for GBS-S<sub>10</sub>, where the heat treatment led to an increase of  $K_{IC}$  from  $2.4\pm 0.3$  to  $2.8\pm 0.3$   $MPam^{1/2}$  for as-deposited and heat-treated state, respectively, despite neglectable changes in Young's modulus (Fig. 27), fracture stress (Fig. 28) and fracture morphology (Fig. 24).

In the available literature, significant toughening was up to now either achieved via complex microstructures [16, 18-19], such as sculptured grains not suitable for industrial sized deposition or by applying metal interlayers [48], which do not have appropriate hot hardness required for dry milling as shown in the case of Cr by Fritz *et al.* [49].

An example is given by Daniel *et al.* [19], where a coating architecture of sculptured TiN layers of 250 nm are divided by SiO<sub>x</sub> interlayers of 20 nm. Thereby, a hierarchical structure closely related to GBS-MI<sub>2</sub> in this thesis was investigated. There, the multi-layered coating yielded at a critical stress intensity factor of  $3.1\pm 0.3$   $MPam^{1/2}$ , significantly higher than  $2.7\pm 0.3$   $MPam^{1/2}$  of GBS-MI<sub>2</sub>. This leads to the conclusion that extrinsic toughening provided by spatial heterogeneity between TiN and SiO<sub>x</sub> is more effective than the approach of toughening by segregation using an interlayer with nearly similar composition.

## Conclusion and Outlook

---

Within the scope of this thesis a gradient coating with a composition  $(\text{Al}_{0,8}\text{Cr}_{0,2})_{1-x}\text{Si}_x\text{N}$  was characterized by correlative cross-sectional nanoanalytics combining CSnanoXRD in WAXD and SAXS geometry, nanoindentation and micromechanical test. It was shown that the addition of Si lead to a defined decrease in grain size, indicated by the increase of the FWHM from 0.3 to 0.45 deg and the formation of a 25 nm layered hierarchical structure revealed by SAXS. Both of these structures persisted through annealing up to 1050°C for 5 min and proved the qualities of the w-Al(Cr)N structure regarding its thermal stability. Furthermore, these changes could be transferred to the mechanical behaviour of the coating as the fracture mode changed from intercrystalline to a nanocomposite glass-like fracture. Thereby, fracture stress was increased from 3.4 to 4.6 GPa and elastic modulus was increased from 208 to 250 GPa, when changing the composition from  $\text{Al}_{0,8}\text{Cr}_{0,2}\text{N}$  to  $\text{Al}_{0,63}\text{Cr}_{0,27}\text{Si}_{0,1}\text{N}$  in the as-deposited state.

Further efforts to increase the coating performance by depositing a hierarchical multilayered structure of Si-alloyed and Si-free sublayers could not increase the mechanical properties above levels of their respective reference coatings and couldn't live up to values found by comparable coatings consisting of TiN and  $\text{SiO}_x$  found in literature [19].

In order to find the reason for the inability to transfer structural properties to actual enhancements of the mechanical properties of the coating further research could possibly use Transmission Electron Microscopy or 3D atom probe tomography to further understand the relationship between these precipitates and their surrounding matrix.

# References

---

- [1] S. Veprek and M. J. G. Veprek-Heijman, "Industrial applications of superhard nanocomposite coatings," *Surf. Coatings Technol.*, vol. 202, no. 21, pp. 5063–5073, 2008.
- [2] J. Vetter, A. O. Eriksson, A. Reiter, V. Derflinger, and W. Kalss, "Quo vadis: AlCr-based coatings in industrial applications," *Coatings*, vol. 11, no. 3, 2021.
- [3] G. List, G. Sutter, and A. Bouthiche, "Cutting temperature prediction in high speed machining by numerical modelling of chip formation and its dependence with crater wear," *Int. J. Mach. Tools Manuf.*, vol. 54–55, pp. 1–9, 2012.
- [4] H. Holleck and V. Schier, "Multilayer PVD coatings for wear protection," *Surf. Coatings Technol.*, vol. 76–77, no. 1995, pp. 328–336, 1995.
- [5] W. Münz, "Titanium aluminum nitride films: A new alternative to TiN coatings," *J. Vac. Sci. Technol. A Vacuum, Surfaces, Film.*, vol. 4, no. 6, pp. 2717–2725, 1986.
- [6] A. Sugishima, H. Kajioka, and Y. Makino, "Phase transition of pseudobinary Cr-Al-N films deposited by magnetron sputtering method," *Surf. Coatings Technol.*, vol. 97, no. 1–3, pp. 590–594, 1997.
- [7] J. Vetter, E. Lugscheider, and S. S. Guerreiro, "(Cr:Al)N coatings deposited by the cathodic vacuum arc evaporation," *Surf. Coatings Technol.*, vol. 98, no. 1–3, pp. 1233–1239, 1998.
- [8] A. E. Reiter, V. H. Derflinger, B. Hanselmann, T. Bachmann, and B. Sartory, "Investigation of the properties of Al<sub>1-x</sub>Cr<sub>x</sub>N coatings prepared by cathodic arc evaporation," *Surf. Coatings Technol.*, vol. 200, no. 7, pp. 2114–2122, 2005.
- [9] M. Kawate, A. Kimura, and T. Suzuki, "Microhardness and lattice parameter of Cr<sub>1-x</sub>Al<sub>x</sub>N films," *J. Vac. Sci. Technol. A Vacuum, Surfaces, Film.*, vol. 20, no. 2, pp. 569–571, 2002.
- [10] P. H. Mayrhofer, H. Willmann, and A. E. Reiter, "Structure and phase evolution of Cr-Al-N coatings during annealing," *Surf. Coatings Technol.*, vol. 202, no. 20, pp. 4935–4938, 2008.
- [11] M. Meindlhumer et al., "Stress-controlled decomposition routes in cubic AlCrN films assessed by in-situ high-temperature high-energy grazing incidence transmission X-ray diffraction," *Sci. Rep.*, vol. 9, no. 1, pp. 1–14, 2019.
- [12] G. Gottstein, *Materialwissenschaft und Werkstofftechnik*, 4. Auflage. Springer Vieweg, 2014.
- [13] D. Raabe et al., "Grain boundary segregation engineering in metallic alloys: A pathway to the design of interfaces," *Curr. Opin. Solid State Mater. Sci.*, vol. 18, no. 4, pp. 253–261, 2014.
- [14] M. Kuzmina, D. Ponge, and D. Raabe, "Grain boundary segregation engineering and austenite reversion turn embrittlement into toughness: Example of a 9 wt.% medium

- Mn steel*,” *Acta Mater.*, vol. 86, pp. 182–192, 2015.
- [15] S. Mandal, K. G. Pradeep, S. Zaefferer, and D. Raabe, “A novel approach to measure grain boundary segregation in bulk polycrystalline materials in dependence of the boundaries’ five rotational degrees of freedom,” *Scr. Mater.*, vol. 81, pp. 16–19, 2014.
- [16] M. Meindlhumer et al., “Biomimetic hard and tough nanoceramic Ti-Al-N film with self-assembled six-level hierarchy,” *Nanoscale*, vol. 11, no. 16, pp. 7986–7995, 2019.
- [17] R. Daniel et al., “Fracture toughness enhancement of brittle nanostructured materials by spatial heterogeneity: A micromechanical proof for CrN/Cr and TiN/SiO<sub>x</sub> multilayers,” *Mater. Des.*, vol. 104, pp. 227–234, 2016.
- [18] R. Daniel et al., “Grain boundary design of thin films: Using tilted brittle interfaces for multiple crack deflection toughening,” *Acta Mater.*, vol. 122, pp. 130–137, 2017.
- [19] R. Daniel et al., “Multi-scale interface design of strong and damage resistant hierarchical nanostructured materials,” *Mater. Des.*, vol. 196, p. 109169, 2020.
- [20] N. Jäger et al., “Microstructural evolution and thermal stability of AlCr(Si)N hard coatings revealed by in-situ high-temperature high-energy grazing incidence transmission X-ray diffraction,” *Acta Mater.*, vol. 186, pp. 545–554, 2020.
- [21] N. Jäger et al., “Evolution of structure and residual stress of a fcc/hex-AlCrN multi-layered system upon thermal loading revealed by cross-sectional X-ray nano-diffraction,” *Acta Mater.*, vol. 162, pp. 55–66, 2019.
- [22] J. Keckes et al., “X-ray nanodiffraction reveals strain and microstructure evolution in nanocrystalline thin films,” *Scr. Mater.*, vol. 67, no. 9, pp. 748–751, 2012.
- [23] A. Kubec, S. Braun, S. Niese, P. Kr, C. G. Schroer, and A. Leson, “Full-field X-ray microscopy with crossed partial multilayer Laue lenses,” vol. 22, no. 17, pp. 20008–20013, 2014.
- [24] J. Kieffer and D. Karkoulis, “PyFAI, a versatile library for azimuthal regrouping,” *J. Phys. Conf. Ser.*, vol. 425, no. PART 20, 2013.
- [25] G. Ashiotis et al., “The fast azimuthal integration Python library: PyFAI,” *J. Appl. Crystallogr.*, vol. 48, pp. 510–519, 2015.
- [26] L. Spieß, G. Teichert, R. Schwarzer, H. Behnken, and G. Christoph, *Moderne Röntgenbeugung: Röntgendiffraktometrie für Materialwissenschaftler, Physiker und Chemiker*. 2019.
- [27] J. Faber and T. Fawcett, “The Powder Diffraction File : present and future research papers,” pp. 325–332, 2002.
- [28] S. Gates-rector, “The Powder Diffraction File : a quality materials characterization database,” vol. 34, no. 4, pp. 352–360, 2019.
- [29] L. Spieß, G. Teichert, R. Schwarzer, H. Behnken, and C. Genzel, *Moderne Röntgenbeugung. Springer Spektrum*, 2019.
- [30] M. Stefenelli et al., “X-ray analysis of residual stress gradients in TiN coatings by a Laplace space approach and cross-sectional nanodiffraction : a critical comparison research papers,” *J. Appl. Crystallogr.*, vol. 46, pp. 1378–1385, 2013.

- [31] G. M. Pharr, J. H. Strader, and W. C. Oliver, "Critical issues in making small-depth mechanical property measurements by nanoindentation with continuous stiffness measurement," *J. Mater. Res.*, vol. 24, no. 3, pp. 653–666, 2009.
- [32] G. M. Oliver and W. C. Pharr, "Measurement of Thin Film Mechanical Properties Using Nanoindentation," *MRS Bull.*, vol. 17, no. (7), pp. 28–33, 1992.
- [33] W. C. Oliver and G. M. Pharr, "Measurement of hardness and elastic modulus by instrumented indentation: Advances in understanding and refinements to methodology," *J. Mater. Res.*, vol. 19, no. 1, pp. 3–20, 2004.
- [34] M. Meindlhumer, "Micromechanical Characterization of Self-Organized Ti<sub>1-x</sub>Al<sub>x</sub>N Nanolamellae: The Influence of Interface Coherency and Phase Alteration on Fracture Behaviour," *Montanuniversität Leoben*, 2016.
- [35] E. Carrera, G. Giunta, and M. Petrolo, *Beam Structures: Classical and Advanced Theories*. 2011.
- [36] D. Gross and T. Seelig, *Bruchmechanik. Springer Spektrum*, 2019.
- [37] H. Tada, P. C. Paris, and G. R. Irwin, *The Stress Analysis of Cracks Handbook*, Third Edition. 2010.
- [38] R. Kelly, "An attempt to understand preferential sputtering," *Nucl. Instruments Methods*, vol. 149, no. 1–3, pp. 553–558, 1978.
- [39] I. Petrov, P. B. Barna, L. Hultman, and J. E. Greene, "Microstructural evolution during film growth," *J. Vac. Sci. Technol. A Vacuum, Surfaces, Film.*, vol. 21, no. 5, pp. S117–S128, 2003.
- [40] M. Hans et al., "Substrate rotation-induced chemical modulation in Ti-Al-O-N coatings synthesized by cathodic arc in an industrial deposition plant," *Surf. Coatings Technol.*, vol. 305, pp. 249–253, 2016.
- [41] R. Daniel, J. Keckes, I. Matko, M. Burghammer, and C. Mitterer, "Origins of microstructure and stress gradients in nanocrystalline thin films: The role of growth parameters and self-organization," *Acta Mater.*, vol. 61, no. 16, pp. 6255–6266, 2013.
- [42] K. J. Martinschitz, R. Daniel, C. Mitterer, and J. Keckes, "Stress evolution in CrN/Cr coating systems during thermal straining," *Thin Solid Films*, vol. 516, no. 8, pp. 1972–1976, 2008.
- [43] P. Hidnert, "Thermal expansion of cemented tungsten carbide," *J. Res. Natl. Bur. Stand.* (1934), vol. 18, no. 1, p. 47, 1937.
- [44] C. Sabitzer, J. Paulitsch, S. Kolozsvári, R. Rachbauer, and P. H. Mayrhofer, "Impact of bias potential and layer arrangement on thermal stability of arc evaporated Al-Cr-N coatings," *Thin Solid Films*, vol. 610, pp. 26–34, 2016.
- [45] A. Drnovšek, H. T. Vo, M. R. de Figueiredo, S. Kolozsvári, P. Hosemann, and R. Franz, "High temperature fracture toughness of single-layer CrAlN and CrAlSiN hard coatings," *Surf. Coatings Technol.*, vol. 409, no. November 2020, 2021.
- [46] P. H. Mayrhofer et al., "Self-organized nanostructures in the Ti-Al-N system," *Appl. Phys. Lett.*, vol. 83, no. 10, pp. 2049–2051, 2003.

- [47] M. Bartosik, C. Rumeau, R. Hahn, Z. L. Zhang, and P. H. Mayrhofer, "Fracture toughness and structural evolution in the TiAlN system upon annealing," *Sci. Rep.*, vol. 7, no. 1, pp. 1–9, 2017.
- [48] A. Zeilinger et al., "Mechanical property enhancement in laminates through control of morphology and crystal orientation," *J. Phys. D: Appl. Phys.*, vol. 48, no. 29, 2015.
- [49] R. Fritz, D. Wimler, A. Leitner, V. Maier-Kiener, and D. Kiener, "Dominating deformation mechanisms in ultrafine-grained chromium across length scales and temperatures," *Acta Mater.*, vol. 140, pp. 176–187, 2017.



# Index of Figures

---

<b>Figure 1:</b> Phase development of fcc AlCrN (a) and w-Al(Cr)N during annealing [10].	5
<b>Figure 2:</b> A schematic view of the CSnanoXRD performed on an exemplary CrN coating [22]	13
<b>Figure 3:</b> A visual display of the Bragg condition of constructive interference on a primitive square lattice.	14
<b>Figure 4:</b> An exemplary array of indents on an $(Al_{0.8}Cr_{0.2})_{1-x}Si_xN$ coating cross-section. The indents range from the WC-Co substrate across the TiN bonding layer throughout coating.	18
<b>Figure 5:</b> The schematic load-displacement curve for the nanoindentation experiment [32].	19
<b>Figure 6:</b> A SEM image of a cantilever prior to testing.	20
<b>Figure 7:</b> Measured compliance as a function of the cantilever compliance.	22
<b>Figure 8:</b> An EDX measurement of the GBS- $Si_x$ gradient coating in the as deposited state, for relevant elemental composition	25
<b>Figure 9:</b> SEM-image of the GBS- $Si_x$ cross section in as-deposited state (a) shows layered microstructure. Further magnification reveals differences at the coating surface (b) and the coating- substrate interface (c).	27
<b>Figure 10:</b> SEM-image of the GBS- $Si_x$ 1000°C cross section (a) shows layered microstructure. Further magnification reveals differences at the coating surface (b) and the coating-substrate interface (c).	28
<b>Figure 11:</b> SEM-image of the GBS- $Si_x$ -1050°C cross section (a) shows layered microstructure. Further magnification reveals differences at the coating surface (b) and the coating substrate interface (c).	29
<b>Figure 12:</b> SEM-image of the GBS- $Si_x$ -1100°C cross section (a) shows layered microstructure. Further magnification reveals differences at the coating surface (b) and the coating-substrate interface (c).	30
<b>Figure 13:</b> (a) A diffraction Intensity from GBS- $Si_x$ ad shows reflections of the wurtzite AlN and cubic CrN phases as well as reflection of the TiN bonding layer. Further analysis of the AlN (100) reflection reveals gradients in FWHM (b) and stress (c).	31
<b>Figure 14:</b> (a) Intensity distribution of GBS- $Si_x$ 1000°C shows maxima of the wurtzite AlN and cubic CrN phase as well as reflections from the TiN bonding layer at higher coating depth. Further analysis of the AlN (100) reflection reveals influences of the heat treatment on FWHM (b) and stress (c).	32
<b>Figure 15:</b> (a) Intensity distribution of GBS- $Si_x$ 1050°C shows maxima of the wurtzite AlN and cubic CrN phases as well as reflections from the TiN bonding layer at higher coating depth. Further analysis of the AlN (100) reflections reveals influences of heat treatment on FWHM (b) and stress (c).	33
<b>Figure 16:</b> (a) Intensity distribution of GBS- $Si_x$ 1100°C shows maxima of the wurtzite AlN and cubic CrN phase as well as reflections from the TiN bonding layer at higher coating depth.	63

<i>Further analysis of the AlN (100) reflection reveals an influence of the heat treatment on FWHM (b) and stress (c).</i>	35
<b>Figure 17:</b> <i>The GBS-Si<sub>x</sub>-ad cross section (a) in addition to the measurement of Si content (b) reveals the formation of a nanolayered structure of a periodicity <math>\Gamma</math> (c) which can be extracted from the correlating SAXS diffractogram in (d).</i>	36
<b>Figure 18:</b> <i>The GBS-Si<sub>x</sub>-1000°C cross section (a) in addition to the measurement of Si content (b) reveals the formation of a nanolayered structure of a periodicity <math>\Gamma</math> (c) which can be extracted from the correlating SAXS diffractogram (d).</i>	37
<b>Figure 19:</b> <i>The GBS-Si<sub>x</sub>-1050°C cross section (a) in addition to the measurement of Si content (b) reveals the formation of a nanolayered structure of a periodicity <math>\Gamma</math> (c) which can be extracted from the cross-sectional SAXS data (d).</i>	38
<b>Figure 20:</b> <i>The GBS-Si<sub>x</sub>-1100°C cross section (a) in addition to the measurement of Si content (b) reveals the formation of a nanolayered structure of a periodicity <math>\Gamma</math> (c) which can be extracted from the cross-sectional SAXS data (d).</i>	39
<b>Figure 21:</b> <i>The indentation modulus was measured as a function of the coating depth by nanoindentation for the GBS-Si<sub>x</sub> gradient coating in as deposited state as well as after annealing.</i>	40
<b>Figure 22:</b> <i>The hardness was measured as a function of the coating depth by nanoindentation.</i>	41
<b>Figure 23:</b> <i>SEM images of a GBS-Si<sub>0</sub>-ad fracture surface (a) with an image of the FIB cut cross section (b) compared to the fracture surface after the heat treatment (c) and corresponding microstructure (d).</i>	42
<b>Figure 24:</b> <i>A SEM image of a GBS-Si<sub>10</sub>-ad fracture surface (a) with an image of the FIB cross section (b) compared to the fracture surface after heat treatment (c) and correlating microstructure (d).</i>	44
<b>Figure 25:</b> <i>A SEM image of a GBS-Ml<sub>1</sub>-ad fracture surface (a) with an image of the fib cut cross section (b) compared to the fracture surface after heat treatment (c) and correlating microstructure (d).</i>	46
<b>Figure 26:</b> <i>A SEM image of a GBS-Ml<sub>2</sub>-ad fracture surface (a) with an image of the fib cut cross section (b) compared to the fracture surface after heat treatment (c) and correlating microstructure (d).</i>	48
<b>Figure 27:</b> <i>Comparison of the elastic modulus of different coating sample systems</i>	51
<b>Figure 28:</b> <i>Comparison of the Fracture Stress of different coating sample systems</i>	52
<b>Figure 29:</b> <i>Comparison of the Fracture Toughness of different coating sample systems</i>	53

# Index of Tables

---

**Table 2:** An overview of the samples investigated in this thesis with their labels and the target composition. 12

**Table 2:** An overview of the different mechanical properties of the two multilayer coatings GBS-ML<sub>1</sub> and GBS-ML<sub>2</sub>, as well as the reference coatings GBS-Si<sub>0</sub> and GBS-Si<sub>10</sub>. 50